The Effect of Annealing on the Microstructures and Oxidation Behaviors of AlCoCrFeNi Complex Concentrated Alloys

Todd M. Butler[1,2], Michael J. Pavel[1], and Mark L. Weaver[1,*]

[1] Department of Metallurgical and Materials Engineering, University of Alabama, Tuscaloosa, AL, 35487-0202, USA
[2] Present address: Air Force Research Laboratory, Materials and Manufacturing Directorate, Wright-Patterson AFB, OH 45433, USA.

Abstract

This paper reports the effects of annealing at 1050°C in an inert atmosphere on the microstructures and high temperature oxidation behaviors of $Al_x(CoCrFeNi)_{1-x}$ CCAs, where x = 8, 12, 15, 20, and 30 (at.%) complex concentrated alloys. In all cases, annealing stabilized multi-phase microstructures consisting of a combination of BCC, B2, and/or FCC phases with the final phase constitution being dependent on the Al content in the alloy. All the alloys exhibited brief periods of transient oxidation, followed by various degrees of parabolic oxide growth. The as-cast alloys, which were observed to predominantly be Cr_2O_3 formers, oxidation resistance increased with increasing Al content. After annealing, all of the alloys transitioned into Al_2O_3 formers but with increased mass gain up to 20 at.% Al. Comparison of the experimental results with thermodynamic models of alloy phase equilibria and oxidation products suggests that an increase in the volume fractions of Al-rich phases near the alloy surfaces as a result of annealing, increases oxidation resistance by providing Al reservoirs for the formation of Al_2O_3. The oxidation mechanisms are discussed relative to existing M-Cr-Al oxide formation models.

* Corresponding author at: Department of Metallurgical & Materials Engineering, The University of Alabama, Tuscaloosa, AL, 35487
E-mail address: mweaver@eng.ua.edu (M.L. Weaver)

1. Introduction

High-entropy alloys (HEAs) and compositionally complex alloys (CCAs) are receiving a substantial amount of scientific interest due to their unique microstructures and often unprecedented combinations of properties [1-6]. Chemically these alloys, which are composed of five or more principal elements (each with a concentration between 5-35 at.%), sit near the centers of their respective phase diagrams [6-8]. Relative to entropy, HEAs inherently exhibit high ideal configurational entropies of mixing ($\Delta S_{mix}^{ideal} \geq 1.5R$), where R is the ideal gas constant. This has been reported to help facilitate the formation of single phase solid solution crystals with high-symmetry, face-centered cubic, body-centered cubic and/or hexagonal close packed crystal structures as opposed to forming a variety of ordered intermetallic phases [4]. In CCAs, two or more stable phases form, some of which might themselves qualify as HEAs and some of which might be ordered intermetallics or other topologically close-packed phases [6,9]. The presence of these high temperature secondary phases has profound influences on mechanical and chemical properties and widens the engineering potential of CCAs over the more rigid HEA class.

Unlike many conventional alloys, HEAs are compositionally diverse and can be alloyed with high concentrations of protective oxide-forming elements such Al, Cr, and/or Si to promote enhanced environmental resistance. With this in mind, there have numerous reports of enhanced oxidation and corrosion resistances in a variety of different HEA and CCA systems [10-27], the majority of which are summarized in references [28-33]. Many of these cases report parabolic oxide growth kinetics, which is ideal for providing protection from oxidation in high temperature, oxidizing environments.

HEAs have also been reported to display sluggish diffusion in comparison to pure metals and less compositionally complex alloys [34-36]. This idea was quantitatively investigated in the

work of Tsai et al. [35], who reported the slowed diffusion rates of Cr, Mn, Fe, Co, and Ni in a CoCrFeMnNi HEA due to higher activation energies for diffusion in the high-entropy lattice. This work was later analyzed by Beke et al. [36], who suggested that temperature insensitive correlation factors, inherent to HEAs due to their compositionally complex lattices, were the more likely cause for the observed behaviors. Regardless of the underlying mechanism, sluggish diffusion would certainly aid in the retention of microstructural stability at high temperatures and could potentially offer synergistic effects with regards to oxidation mechanisms. From a design standpoint, all these factors make HEAs attractive candidates for use in high temperature applications.

The present study was initiated to elucidate the influence of annealing on the microstructures and high temperature oxidation behaviors of AlCoCrFeNi CCAs. The experimental results are compared with previously published results for as-cast AlCoCrFeNi CCAs [37,38], relevant conventional alloys, and existing oxide formation models. This study follows up a preliminary investigation of the post-annealing oxidation behaviors of three alloys containing 8, 15, and 30 at.% Al with near equiatomic concentrations of the remaining elements [39]. In the current work, thermodynamic modeling via the CALPHAD method has been used to substantiate the observed microstructures and oxidation mechanisms.

2. Materials and Methods

Five CCAs with the compositions (at.%) of $Al_8(CoCrFeNi)_{92}$, $Al_{12}(CoCrFeNi)_{88}$, $Al_{15}(CoCrFeNi)_{85}$, $Al_{20}(CoCrFeNi)_{80}$, and $Al_{30}(CoCrFeNi)_{70}$ (designated: Al_8, Al_{12}, Al_{15}, Al_{20}, and Al_{30}) were synthesized into bulk buttons via non-consumable arc-melting on a water-cooled copper hearth under an inert argon atmosphere. To promote homogeneity, each alloy button was flipped and re-melted at least five times. The alloy compositions, as determined using energy-dispersive

x-ray spectroscopy (EDS) are shown in Table 1 and were consistent with the target nominal alloy compositions.

Oxidation specimens were cut from the bulk buttons for annealing using a low speed diamond saw. The specimens were approximately 3 mm thick. The specimens were ultrasonically cleaned in baths of acetone, methanol, ethanol, and isopropanol. Specimens were annealed at 1050°C for 120 hours in a tube furnace under flowing ultra-high purity (UHP) argon, followed by water quenching.

Microstructural analysis was conducted using a combination of scanning electron microscopy (SEM), EDS, transmission electron microscopy (TEM), and x-ray diffraction (XRD). EDS was performed in both SEM and TEM modes. Specimens for TEM analysis were made using a variation of the focused-ion-beam (FIB) in situ lift-out method for TEM foil preparation in an FEI Quanta 200 3D Dual Beam FIB-SEM [40]. Plan view and cross-sectional images of the annealed and oxidized HEAs were captured on a JEOL 7000F SEM in backscattered electron (BSE) and secondary electron (SE) modes. High angle annular dark field (STEM-HAADF) images and selected area diffraction patterns (SADPs) were captured on a 200-KeV FEI Tecnai G^2 F-20 Supertwin scanning-transmission electron microscope STEM. TEM-EDS data was evaluated using FEI ES Vision software with an applied thickness correction [41]. XRD spectra were collected from bulk samples using a Philips X'pert™ MPD XRD with Cu-Kα radiation at 45 kV and 40 mA.

Specimens were subjected to discontinuous, isothermal oxidation testing at 1050°C under ambient laboratory air. Prior to testing, all specimens were ground with SiC paper to a 1200 grit surface finish followed by ultrasonic cleaning. To quantify the oxidation behaviors, samples were manually removed from the furnace during testing and periodically weighed using an Orion Cahn

C-34 microbalance (10^{-6} g sensitivity). The post oxidation microstructures were investigated using the previously defined analytical techniques.

The annealing temperature of 1050°C used in this study was selected based upon thermodynamic model predictions using the CALPHAD method. This annealing temperature was selected to promote the formation of stable two- or three-phase microstructures consisting of mixtures of FCC, BCC, and or long-range ordered B2 phases whilst avoiding the formation of deleterious TCP phases. As a primary goal of this investigation was to explore the formation of Al_2O_3, an oxidation temperature of 1050°C was selected because it lies just above the regime where Cr volatilization would be expected [42,43]. The modeling of oxidation phase evolution was explored at the same temperature using pure oxygen as the oxidant to match TGA test conditions. All calculations were conducted in ThermoCalc™ and utilized the TCNI9 (Ni-based superalloy) and TCHEA4 (high entropy alloy) databases. Additionally, predicted phase chemistries and relative phase fractions were compared to those determined experimentally. The experimental phase fractions for each phase were determined in the annealed states using a 2D image analysis technique with ImageJ software [44]. The respective phases were quantified into areas based on their average atomic number Z contrast. This was then converted to a three dimensional volume fraction through an equivalent spherical volume technique [45].

3. Results and Discussion

3.1 Microstructures and Phase Distributions of the Annealed HEAs

Figs. 1 through 5 summarize the annealed microstructures, CALPHAD predicted phase fractions as a function of temperature, and experimentally determined phase fractions after annealing at 1050°C for the five CCAs examined in this study. Table 1 summarizes the alloy and phase compositions observed after annealing. Not surprisingly, all the alloys consisted of multiple

phases with the phase contents and volume fractions being dependent upon alloy composition. As expected, the phases in each sample appeared to be more uniformly distributed after the heat treatment. All the alloys were also found to contain less than 1 vol. % AlN inclusions which were attributed to impurities in the starting materials and/or the arc-melting process.

The annealed $Al_{8,}$ Al_{12}, and Al_{15} CCAs (Figs. 1-3) were found to consist of two phases; a continuous, high atomic number (high-Z) contrast matrix phase (labeled FCC) that encompassed a low atomic number (low-Z) contrast precipitate phase (labeled B2). In general, the precipitates exhibited plate-like morphologies and appeared to increase in size and volume fraction with increasing Al content. Chemical and structural analysis in the TEM showed the matrix phase to be rich in Co, Cr, and Fe with a disordered FCC crystal structure, and the precipitate phase to be rich in Ni and Al with an ordered B2 crystal structure (Figs. 1 – 3 and Table 1). These observations, along with the experimental phase chemistries and volume fractions are consistent with the thermodynamic predictions of FCC and B2 phases at 1050°C (Table 1 and Figs. 1(e, f), 2(e, f), and 3(e, f)).

The annealed Al_{20} HEA was found to consist of three distinct phases (Fig. 4); a semi-continuous high-Z phase along grain boundaries (labeled FCC), that encompassed multiphase regions consisting of a continuous low-Z matrix phase (labeled B2) interspersed with discontinuous high-Z and medium-Z contrast regions (labeled BCC + B2). The high-Z regions exhibited the same Z contrast and chemistries as the grain boundary phase; whereas the medium-Z regions were composed of a higher Z matrix intermixed with low-Z cube shaped precipitates. Much like the lower Al content alloys described above, the matrix phase was found to be rich in Ni and Al with an ordered B2 crystal structure. The high-Z grain boundary and precipitate phases were found to be extremely rich in Co, Cr, and Fe with disordered FCC crystal structures. The

medium-Z regions were also rich in these elements but were found to consist of a mixture of uniform, disordered BCC zones and disordered BCC regions that contained very fine rich B2 precipitates (Fig. 4(b)). Similar microstructures have been reported by Wang et al. [46-48] in comparable alloys.

The calculated phase diagram for the annealed Al_{20} CCA predicts a 1050°C equilibrium microstructure consistent with experimental observations, composed of B2 and BCC phases in approximately a 3:1 ratio and a 0.7% FCC phase (Fig. 4(g)). The calculated phase fractions along with those predicted via thermodynamic modeling are shown in Fig. 4(h). The predictions tend to correlate well with the calculated volume fractions of each of the three phases. The thermodynamically predicted phase chemistries correlated well with those determined via EDS (Table 1). When comparing the modeling predictions for the Al_{15} and Al_{20} CCAs, Figs. 3(e) and 4(g), it can be inferred that increasing the Al content tends to decrease the fraction of the FCC phase, while simultaneously increasing the fraction of the BCC phase. The FCC phase is almost entirely destabilized at ~ 20 at.% Al, which explains the small mole fraction of the FCC phase in the Al_{20} predictions.

Fig. 5(a) shows a BSE image of the annealed Al_{30} CCA. The microstructure consisted of a fine-scale, high-Z Cr+Fe rich phase (labeled BCC) with a dispersion of low-Z, Ni+Al-rich phase (labeled B2). The structures were investigated using TEM, as shown by the STEM-HAADF image and SADPs in Figs. 5 (b)-(d). Like the Al_{20} CCA, the low-Z matrix phase was uniform and exhibited a B2 structure. The high-Z phase was composed of a disordered BCC matrix and contained regions occupied by nano-scale Ni+Al-rich B2 precipitates (Fig. 5(b)). In addition, the precipitates were not adequate in size for routine electron diffraction identification. However, these precipitate distributions are consistent with those observed by Wang et al. [46-48].

Fig. 5(e) shows the calculated phase diagram for the Al_{30} CCA. At 1050°C, the Al_{30} CCA is predicted to have an equilibrium microstructure consisting of a mixture of B2 and BCC phases in nearly a 4:1 ratio. The calculated phase fractions, along with those thermodynamically predicted, are shown in Fig. 5(f). The predicted stable phases and phase fractions are fully consistent with those observed experimentally. Additionally, the thermodynamically predicted phase chemistries were also consistent with those determined via SEM-EDS, as shown in Table 1.

3.2 Post Oxidation Microstructures

To elucidate the influence of annealing on the active oxide formation mechanisms, the post oxidation microstructures of the annealed CCAs were investigated and compared with recent results for cast alloys with the same compositions [37,38]. In contrast to the as-cast alloys, all the annealed alloys exhibited a high degree of oxide scale spallation during oxidation testing. Figs. 6 and 7 show representative BSE images of the oxidized microstructures after 50 hours at 1050°C in air. As-cast alloys formed continuous, external Cr_2O_3 scales with underlying Al_2O_3 scales, as shown in Figs. 6(a)-(e). The morphology of the internal Al_2O_3 scale was found to be highly dependent on the relative Al concentration in the alloy. The as-cast Al_8 CCA formed an intermediate metal layer under the outer Cr_2O_3 scale followed by a discontinuous internal Al_2O_3 scale, as shown in Fig. 6(a). The as-cast Al_{12} and Al_{15} CCAs formed a semi-continuous internal Al_2O_3 scale directly beneath the outer Cr_2O_3 scale. The highest Al content alloys (as-cast Al_{20} and Al_{30}) tended to form fully continuous internal Al_2O_3 scales, which should inherently exhibit the most superior oxidation resistances. This evolution of Al_2O_3 scale morphology is shown schematically in Fig. 6 (f). With increased Al content, the continuity of the internal Al_2O_3 scale increases, until it becomes entirely continuous at high Al concentrations. Some AlN precipitates were also detected near the internal Al_2O_3 scales. Krupp et. al [49] observed a similar formation

of nitrides during the oxidation of single-crystal nickel-based superalloys in air. Additionally, these post oxidation microstructures are also comparable to those observed in the works of Hall et al. [50] on the oxidation of model FeNiCrAl alloys at 900°C and Zhang et al. [13] on the oxidation behavior of $Al_{0.5}FeCoCrNi$ and $Al_{0.5}CoCrFeNiSi_{0.2}$ HEAs.

The annealed CCAs were found to display vastly different oxidation mechanisms than the as-cast HEAs. Fig. 7 shows representative BSE images of the annealed CCAs after 50 hours at 1050°C in air. In all cases, the annealed alloys formed external Al_2O_3 scales. As depicted in Figs. 7 (a)-(d), the annealed Al_8, Al_{12}, Al_{15}, and Al_{20} alloys also formed an underlying spinel phase that contained nearly equal amounts of Co, Cr, and Fe. Interestingly, this spinel phase was not observed in the annealed Al_{30} HEA, as shown in Fig. 7 (e). The oxidation mechanisms for the annealed CCAs are shown schematically in Fig. 7 (f). In general, the annealed CCAs were found to exhibit external Al_2O_3 scales with underlying spinel phases up to ~20 at.% Al. However, the annealed alloys containing higher Al concentrations exclusively formed Al_2O_3. It is proposed that the Al_2O_3 forms first, which then leads to an Al depleted zone beneath the scale with prolonged oxidation time. This depleted zone eventually reaches a minimum concentration below what is required to sustain the growth of Al_2O_3, thus facilitating the formation of the underlying spinel phase. This is likely preferred due to the presence of high concentrations of Fe, Co, and Cr in these regions. This can be visualized in Fig. 8, which shows a plot of the Al content in the depleted zones versus Al content in each of the CCAs. As expected, the Al content in the Al_8, Al_{12}, Al_{15}, and Al_{20} alloys is very low (less than 4 at.%). In contrast, the measured Al content in the Al_{30} depleted zone is more than 5 at.% higher. For reference, the range of minimum Al concentrations required for the formation of Al_2O_3 formation in Ni-Cr-Al alloys is shown (approximately 5-8 at.% Al). It is not too surprising that the spinel phase was not observed in the annealed Al_{30} alloy during the oxidation

exposure period. It is also expected that the oxidation resistance of the annealed Al_{30} alloy should be far superior in comparison to the other annealed alloys.

The 50 hours oxidized phase structures of the as-cast and annealed CCAs were investigated using XRD, as shown in Figs. 9 (a) and (b), respectively. Patterns were collected in plan-view from the free surfaces of the oxidized samples. As expected, the as-cast alloys displayed peaks associated with FCC, BCC/B2, Cr_2O_3, and Al_2O_3 phases. Similarly, the annealed alloys contained peaks primarily from FCC, BCC/B2, Al_2O_3, and spinel phases. There were also some peaks associated with Cr_2O_3 observed in the annealed HEAs. These structural observations are consistent with the microstructural SEM and TEM findings.

3.3 Thermodynamically Predicted Oxides

Thermodynamic modeling is versatile tool in novel alloy development since it has the potential to reduce the number of necessary experiments. There are many studies in the literature that assess the usefulness and merit of CALPHAD based thermodynamic models for predicting the phases that will form in HEAs and CCAs [51-54]. This work utilizes the same thermodynamic approach with ThermoCalc^{TM} to predict the thermally grown oxides that form on the annealed CCAs. The methodology is based on the work of Klein et al. [55], who examined the oxide formation in Co-Al-W superalloys. They were able to predict stable phases, including oxides, at high temperatures by isothermally varying oxygen activity with a set alloy chemistry and observing the system at an equilibrium state. This simulates the phases that could form during oxidation testing at high temperatures. When the oxygen activity is high, the outermost surface scale of the oxidized alloy is mimicked. Similarly, as the oxygen activity is periodically decreased, one is merely simulating the phases that could potentially form deeper into the alloy where much less oxygen is present. Salam et al. [56] used a similar approach to investigate CoNiCrAlReY

alloys. This does not take into effect the local composition variation and depletion due to selective oxidation but provides a reasonable estimate of global oxidation phenomena.

Figs. 10, 11, and 12 show BSE images of the annealed CCAs after 50 hours of oxidation, along with thermodynamically calculated phase diagrams depicting the stable phases at 1050°C with varied oxygen activities. For reference, the BSE images are rotated 90 degrees clockwise in order to be consistent with the thermodynamic plots (left side: alloy; right side: outer oxide). For all the oxidized alloys, a similar distribution of phases was predicted, as shown in Figs. 10(b), 11(b), and 12(b). The inner alloys near the surface (lowest oxygen activities) were predicted to consist of FCC + B2 phases for the $Al_8 - Al_{15}$ HEAs, and a mixture of BCC + B2 phases for the $Al_{20} - Al_{30}$ HEAs. These predictions are consistent with the phase diagrams shown in Figs. 1-5. As the oxygen activity is increased from ~10^{-14} to 10^{-8}, a combination of Al_2O_3 + FCC phases are predicted to form for all the alloys, including those with little to no FCC phase (Al_{20} and Al_{30}. At high oxygen activities (> 10^{-8}) a mixture of spinel and halite phases is predicted to form for the Al_8, Al_{12}, Al_{15}, Al_{20} and Al_{30} HEAs. As anticipated, the predictions show an increased phase fraction of Al_2O_3 with higher Al content. Interestingly, the relative range (i.e., simulated depth into the alloy) of Al_2O_3 formation with varied oxygen activity remains nearly constant for all the CCAs (~10^{-14} to 10^{-8}) as seen in Fig. 13(a). In contrast, the spinel phases for the Al_8, Al_{12}, Al_{15}, and Al_{20} alloys rise sharply to equilibrium at nearly the same oxygen activity (~10^{-8}) while the Al_{30} alloy shows a much more gradual increase in spinel phases with the static equilibrium being achieved a full magnitude of oxygen activity higher (~10^{-7}), albeit at a higher mole fraction (Fig. 13(b)). This early mole fraction contribution is from the CoCrAlO rich spinel while the secondary NiFeO spinel stabilizes around ~10^{-5} and is nearly identical for all compositions. This higher barrier for formation may be the cause for the Al_{30} samples lack of spinel layer.

As described in section 3.2, a mixture of Al_2O_3 and spinel phases were experimentally observed for nearly all the annealed CCAs, with no spinel detected in the Al_{30} alloy. The thermodynamic models do predict the formation of an outer spinel with an internal sublayer of Al_2O_3, but the experimental observations show that Al_2O_3 tended to form externally, while the spinel phase generally formed internally. The predicted halite phases were not experimentally observed in any of the cases but may have formed during the initial stages of oxidation and either transformed or potentially spalled off. However, these discrepancies can be explained by a lack of kinetics and local chemistry changes in the model. Diffusion plays a key role in determining the oxide products during prolonged oxidation, which in some cases may not be representative of an equilibrium microstructure, as predicted by the model in this work. Similarly, mass transport of atomic species readily occurs during oxidation, leaving Al and/or Cr lean depleted zones beneath the outer scales of Al_2O_3 and Cr_2O_3 formers, respectively. Using previously measured depleted zone (D.Z.) alloy chemistries the same oxidation profiles were calculated to observe changes in the equilibrium phases [38]. While there appeared to be no appreciable change to the spinel forming region, the corundum forming regions of each alloy had a substantial shift (Fig. 14). A decrease in mole fraction of alumina was observed for each alloy, including the Al_{30} specimen, to below that of the lowest aluminum containing base alloy (B.A.). For the Al_8 and Al_{12} samples, less than 0.02 mole fraction of alumina was predicted over the entire oxygen activity range. While the chromia forming region was less effected by depletion, the mole fraction still decreased for each alloy. This seems to confirm the belief that as local aluminum depletion occurs during oxidation, there is simply not a large enough region of stability of alumina to keep forming protective oxide scales. Combining data from the base alloy and depleted zone, ThermoCalc predictions allow for the creation of an oxidation road map which may help describe the initial

stages of oxidation, as well as where the equilibrium is shifting towards as oxidation progresses (Fig. 15). While more simultaneous calculations would improve these predictions, the results of this work show that thermodynamics-based models still serve as useful guides in predicting oxide formation in compositionally complex alloys.

3.4 Oxidation Behaviors

To quantitatively address the influence of annealing on the oxidation behaviors, mass measurements were taken periodically during the oxidation testing of the as-cast and annealed CCAs, as shown in Figs. 16(a) and (b), respectively. All the CCAs displayed some level of initial transient oxidation (typically between 1-5 hours) followed by various degrees of protective, parabolic oxide growth. This behavior is typical of model Ni-Cr-Al alloys and some wrought Ni-based superalloys [57,58]. Several of the as-cast CCAs appeared to statistically plateau after around 10-20 hours, likely indicating the strong volatilization of Cr_2O_3 [43]. The as-cast alloys also exhibited a strong dependence of Al concentration on the relative mass changes, as shown in Fig. 16(a). In general, increasing the Al concentration was observed to enhance the oxidation resistances by reducing the observed total mass gain during oxidation. Microstructurally, higher Al concentrations in the as-cast CCAs facilitated an increase in the continuity of the internal Al_2O_3 scale, which is known to improve the oxidation resistances of model Ni-Cr-Al alloys [58].

For the annealed CCAs, Fig. 16(b), the magnitudes of the mass changes were comparable to those in the as-cast CCAs. The differences in the relative differences in mass change for alloys containing 8 to 20 at.% Al were smaller than their as-cast counterparts, but their total mass gains had some hierarchical structure with the lowest Al content alloys exhibiting larger mass gains than their more concentrated counterparts. In terms of microstructure, the as-cast alloys solidified with a higher volume fraction of FCC phase than would be expected under equilibrium conditions,

which is likely to exclusively form external Cr_2O_3 [38]. During annealing, as the equilibrium volume fraction of Ni+Al-rich B2 phase is obtained, these regions act as Al reservoirs, forcing competition between the two stable oxides, resulting in external Al_2O_3 growth with underlying spinel. In contrast, the Al_{30} HEA displayed post-annealing mass gains that were virtually identical to those in as-cast alloy. This alloy additionally did not form an underlying spinel during the total oxidation exposure time. This is attributed to the presence of higher volume fractions of Ni+Al-rich B2 phase in both conditions which promoted the formation of a more continuous Al_2O_3 subscale in as-cast alloys and in a continuous external Al_2O_3 scale after annealing [23,38].

In general, the annealed alloys displayed longer adherences to parabolic oxide growth (up to ~ 80 hours of oxidation), which can likely be attributed to the absence of Cr_2O_3 in the oxide scales. The calculated parabolic oxide growth constants (k_P), along with their respective adherence times, are shown in Table 2 for the as-cast and annealed CCAs. In the cases where multiple stages of oxidation were observed, additional parabolic oxide growth rate constants were determined. All the rate constants were in the range of ($\sim 10^{-11}$ to 10^{-13}). Only small differences in k_P were observed between the as-cast and annealed alloys. This is somewhat surprising, since the oxidation mechanisms were quite different between the two conditions. However, the observed oxidation behaviors are favorable and indicate that all the CCAs in this study display some degree of oxidation resistance.

3.5 Comparison with Model M-Cr-Al Oxide Formation Models

The oxidation behaviors of the CCAs in this work share distinct similarities with those observed in model M-Cr-Al alloys, where M = Ni, Fe, and Co [58-62]. Depending on the specific alloy chemistry, a variety of different oxidation mechanisms can occur [58,59]. Stott et al. [59] deduced a total of eight different oxidation mechanisms when comparing the oxidation behavior

of all three alloy systems, ranging from exclusive α-Al_2O_3 formation in type 1, to a combination of outer MO/M_2O_3 scales with underlying complex (M+Cr+Al) oxides in type 8. The as-cast CCAs in this study tended to oxidize in manner consistent with type 2 and/or type 3 mechanisms. For type 2 oxidation, an external Cr_2O_3 scale forms with an underlying continuous subscale of Al_2O_3, accompanied by some internal Al_2O_3 precipitates. This behavior correlates well with the as-cast high Al content CCAs (≥ 15 at.%). Similarly, type 3 oxidation occurs by the formation of an outer Cr_2O_3 scale with internal, discontinuous Al_2O_3 precipitates. This closely matches the oxidation behavior in the as-cast low Al content CCAs (< 15 at.%). As for the annealed CCAs, all the observed oxidation behaviors appear to be a variation of type 1 since they all form an outer scale of α-Al_2O_3. However, as was previously described, nearly all of the annealed CCAs also formed underlying spinel phases, which are not adequately described by such models.

Giggins and Pettit also proposed oxide formation mechanisms for the Ni-Cr-Al system, which are established into three distinct groups [58]. Group I alloys form a combination of NiO and spinel phases due to dilute concentrations of both Cr and Al. Group II alloys, with high concentrations of Cr and dilute amounts of Al, form external Cr_2O_3 scales with internal, discontinuous subscales of Al_2O_3. The most oxidation resistant alloys, Group III, form continuous external Al_2O_3 scales with or without minor Cr_2O_3. These three groups are shown plotted on a schematic oxide formation map in Fig. 17(a), along with the relative chemical locations of the CCAs in this study [58,62-64]. For comparison with the Ni-Cr-Al system, Fe+Co+Ni are combined into one term. In general, all the CCAs tend to sit in Group III. However, the Al_8 and Al_{12} alloys sit near the boundary between Groups II and III. Microstructurally, the low Al content (≤ 15 at.%) as-cast CCAs oxidized in a manner consistent with model Group II Ni-Cr-Al alloys. These alloys formed an outer Cr_2O_3 scale with an underlying, discontinuous Al_2O_3 scale. As for

the high Al content as-cast CCAs, the oxidation behavior tended to follow Group III behavior. These alloys formed a continuous Al_2O_3 scale below an outer Cr_2O_3 scale. For the annealed CCAs, all the post oxidation microstructures were similar to Group III behavior, with the formation of a continuous, external Al_2O_3 scale. These alloys also formed an internal spinel, which is inconsistent with Ni-Cr-Al oxide formation models. However, spinel phases of this type commonly form on the outermost surfaces during the initial transient stages of oxidation in Ni-Cr-Al alloys [58].

Quantitatively, the calculated k_P values for the as-cast and annealed CCAs in this study are also consistent with those observed for model Group II and Group III Ni-Cr-Al alloys [58]. The k_P values are shown plotted in Fig. 17(b), along with the respective ranges for both model Group II (Cr_2O_3 formers) and Group III (Al_2O_3 formers). The low Al content alloys (< 20 at.%) tend to sit in Group III, while the high Al content alloys (≥ 20 at.%) sit in the transition zone between Groups II and III. These similarities show the usefulness and merit of existing oxide formation models for predicting the oxidation behaviors of more compositionally complex alloys.

3.6 Comments on Annealing, Modeling, and Oxidation Tendencies

Annealing was found to stabilize multiphase microstructures for all the alloys. This included a mixture of FCC, BCC, and/or B2 solid solution phases depending on the alloy chemistries. The experimentally determined phase fractions and phase chemistries were, in general, consistent with those predicted via thermodynamic modeling. This demonstrates the merit and usefulness of thermodynamic models for predicting the behavior of compositionally complex alloys. This may infer that the annealed CCAs are near an equilibrium state, seemingly unhindered by slow diffusion. Therefore, the true extent of the proposed sluggish diffusion in CCAs remains unknown.

Pre-annealing the CCAs before oxidation testing vastly modified their oxidation behaviors in comparison to the as-cast alloys. During oxidation, the as-cast alloys first formed an external scale of Cr_2O_3. This was followed by the formation of internal Al_2O_3 with various degrees of continuity depending on the alloy chemistry and oxidation time. As previously explained, this mechanism is analogous to the sequential oxidation behavior in model Ni-Cr-Al alloys. It is not surprising that the as-cast CCAs displayed a strong dependence between Al content and overall oxidation resistance. However, this was observed to promote limited adherences to parabolic oxide growth, and in some cases the mass change curves displayed plateaus and even negative deviations with prolonged oxidation testing likely due to the volatilization of Cr_2O_3. In contrast, annealing of the CCAs was found to increase the fraction of Ni+Al-rich B2 phase, which likely promoted a higher surface area of Al-rich phase at the free surface during oxidation. This changed the oxidation mechanism by providing an Al-reservoir to facilitate the formation of Al_2O_3 first during oxidation. This was later followed by the formation of a spinel beneath the external Al_2O_3 scale in all the annealed CCAs, aside from the Al_{30}. As described previously, below the external Al_2O_3 scale, the localized depletion of Al and the presence of high concentrations of Fe, Co, Cr, and Ni promoted the stability of the observed spinel phase. Correspondingly, it is suggested that the spinel phase was not experimentally observed in the annealed Al_{30} HEA due to the high Al content and insufficient depletion of Al beneath the external Al_2O_3 scale, Fig. 8. The external Al_2O_3 scale formation in the annealed CCAs promoted extended adherences to parabolic oxide growth, with little variability in mass changes up to 20 at.% Al. However, the annealed Al_{30} HEA displayed much better oxidation resistance. This is due to the high Al content, which promoted exclusive Al_2O_3 formation.

In general, thermal annealing promoted the development of microstructures containing more uniform phase distributions, making the annealed alloys less susceptible to aberrations in oxidation behavior and mechanical properties than their as-cast or as as-sintered counterparts [65,66]. Similar observations have been made regarding the influences of phase distributions, in particular Ni+Al-rich-B2 phases, on the aqueous corrosion behaviors of AlCoCrFeNi and $Al_{0.3}$CoCrFeNi alloys [67,68]. The present study, like our prior work, used arc melted alloys which had very large starting grain sizes. New processing methods such as powder metallurgy with spark plasma sintering, cold-spray deposition, and friction-stir related processing may prove beneficial for altering or grain size and phase distributions (see [33,69-73]); however, our results suggest that a proper heat treatment will still be required to fully optimize the phase distributions to deliver improved and consistent oxidation resistance.

Thermodynamic models were utilized to predict the oxide formation in the annealed CCAs. The specific method employed in this work was derived from the work of Klein et al. [55] on Co-Al-W superalloys. In general, the predicted phases were like those observed experimentally, including the formation of Al_2O_3 and spinel phases. The thermodynamic predictions also captured an increased phase fraction of Al_2O_3 scales with higher Al concentrations. Interestingly, the range of Al_2O_3 phase stability appears to be constant regardless of the HEA chemistry (oxygen activity: ~10^{-14} to 10^{-8}). The model also predicted several spinel phases and halite, which were not fully consistent with the experimental observations. It is essential to remember that these predictions are based solely on thermodynamic quantities and lack any kinetic contributions. Furthermore, the models have not yet been adapted to dynamically consider localized chemistry changes (i.e. depleted zones), which can vastly change the equilibrium phases. Computing the oxidation phase diagrams while incorporating the chemistry changes that occur beneath the alumina layer during

oxidation may clarify the reaction pathway and improve predictability. While there is still much to improve upon this work does demonstrate the usefulness and merit of models based exclusively on thermodynamic factors for predicting the oxidation behaviors of AlCoCrFeNi based CCAs.

One of the primary goals of this work was to examine and potentially predict the oxidation behavior of AlCoCrFeNi based CCAs. As described in section 3.5, the post oxidation microstructures compare relatively well with those developed by Stott et al. [59] and Giggins and Pettit [58] for conventional M-Cr-Al (M = Ni, Co, Fe) alloys. This demonstrates that existing oxide formation models for simple, well-developed alloy systems have an immense applicability to compositionally complex HEA systems. It is predicted that HEA systems consisting of various other elements should have compatibility with relevant oxide formation models based on simple alloys with like compositions. This work also demonstrates that AlCoCrFeNi based CCAs tend to selectively oxidize to form Al_2O_3 and/or Cr_2O_3 when alloyed with sufficient quantities of Al and Cr. Thus, from a materials design standpoint, CCAs should be able to be chemically modified to facilitate the formation of microstructures adequate for mechanical loading, while also maintaining a high degree of oxidation/corrosion resistance.

4. Conclusions

This work examined the effect of annealing on the microstructures and high temperature oxidation behaviors of $Al_x(CoCrFeNi)_{1-x}$ CCAs, where x = 8, 12, 15, 20, and 30 (at.%). The following key points can be made:

1) Annealing at 1050°C for 120 hours promoted multi-phase microstructures in all the CCAs. In general, the low Al content CCAs (≤ 15 at.%), formed a combination of FCC and B2 phases, while the high Al content CCAs (≥ 20 at.%) formed a mixture of BCC and B2 phases. The Al_{20} HEA was the only three-phase alloy and formed BCC, B2, and FCC

phases. Higher Al concentrations tended to destabilize the FCC phases and lead to increased phase fractions of both BCC and B2 phases. The experimentally determined phase fractions and chemistries were generally consistent with those predicted by CALPHAD based thermodynamic models using the TCHEA4 database.

2) All of the CCAs were subjected to discontinuous, isothermal oxidation tests at 1050°C and displayed initial transient oxidation (typically between 1-5 hours), followed by various levels of parabolic oxide growth. The alloys oxidized from as-cast states formed outer Cr_2O_3 scales with underlying Al_2O_3 scales. The alloys oxidized from annealed states tended to form a combination of external Al_2O_3 scales with internal spinel phases. The post oxidation microstructures were found to be similar to those predicted by the oxide formation mechanisms proposed by Stott et al. [59] for M-Cr-Al alloys (where M = Ni, Co, and Fe) and those proposed by Giggins and Pettit [58] for model Ni-Cr-Al alloys. The thermodynamically predicted oxides were not completely consistent with those observed experimentally. It is expected that a higher degree of consistency will be obtained once kinetic components and localized chemistry changes can be implemented in the model. However, the models can still provide useful insight when developing compositionally complex alloys for oxidizing environments.

3) The oxidation behaviors of the CCAs in this work are favorable and indicate various degrees of oxidation resistance. The calculated parabolic oxide growth constants (k_P) for the as-cast and annealed alloys correlated well with those observed for Group II and Group III model Ni-Cr-Al alloys. Unlike the annealed alloys, the Al concentration in the as-cast HEAs had a significant impact on the relative oxidation behaviors. Increased Al contents tended to lower the overall mass change curves. However, the order of magnitude of the

mass changes between corresponding as-cast and annealed CCAs was nearly the same. There were only minute differences in k_P values observed between as-cast and annealed states. In all cases, annealing stabilized the microstructures and promoted the formation of an external continuous α-Al_2O_3 scale. The annealed CCAs also exhibited longer adherences to protective, parabolic oxide growth.

4) This work demonstrates the immense applicability of conventional oxide formation models for predicting the oxidation behavior in CCAs. It is predicted that the oxidation behaviors in other HEA systems may share close similarities with existing oxide formation models derived from relevant and compositionally simple alloys.

CRediT authorship contribution statement

Todd M. Butler: Conceptualization, Investigation, Methodology, Writing – Original Draft, Writing – Reviewing & Editing. **Michael Pavel:** Investigation, Writing – Review & Editing. **Mark L. Weaver:** Conceptualization, Methodology, Writing – review & editing, Supervision, Funding acquisition, Project administration.

Acknowledgements

This work utilized equipment owned by the Alabama Analytical Research Center (AARC), which is housed at the University of Alabama. This work was supported by the National Science Foundation (DMR-2105364).

References

[1] D. B. Miracle, J. D. Miller, O. N. Senkov, C. Woodward, M. D. Uchic and J. Tiley, "Exploration and development of high entropy alloys for structural applications," *Entropy,* 16 (2014) 494-525. (doi: https://doi.org/10.3390/e16010494)

[2] J.-W. Yeh, "Alloy Design Strategies and Future Trends in High-Entropy Alloys," *JOM,* 65 (2013) 1759-1771. (doi: https://doi.org/10.1007/s11837-013-0761-6)

[3] J. W. Yeh, Y. L. Chen, S. J. Lin and S. K. Chen, "High-Entropy Alloys-A New Era of Exploitation," *Materials Science Forum,* 560 (2007) 1-9. (doi: https://doi.org/10.4028/www.scientific.net/MSF.560.1)

[4] Y. Zhang, T. T. Zuo, Z. Tang, M. C. Gao, K. A. Dahmen, P. K. Liaw and Z. P. Lu, "Microstructures and properties of high-entropy alloys," *Progress in Materials Science,* 61 (2014) 1-93. (doi: http://dx.doi.org/10.1016/j.pmatsci.2013.10.001)

[5] O. N. Senkov, D. B. Miracle, K. J. Chaput and J.-P. Couzinie, "Development and exploration of refractory high entropy alloys - A review," *Journal of Materials Research,* 33 (2018) 3092-3128. (doi: https://doi.org/10.1557/jmr.2018.153)

[6] D. B. Miracle and O. N. Senkov, "A critical review of high entropy alloys and related concepts," *Acta Materialia,* 122 (2017) 448-511. (doi: http://dx.doi.org/10.1016/j.actamat.2016.08.081)

[7] J. W. Yeh, S. K. Chen, S. J. Lin, J. Y. Gan, T. S. Chin, T. T. Shun, C. H. Tsau and S. Y. Chang, "Nanostructured high-entropy alloys with multiple principal elements: Novel alloy design concepts and outcomes," *Advanced Engineering Materials,* 6 (2004) 299-303. (doi: https://doi.org/10.1002/adem.200300567)

[8] B. Cantor, I. T. H. Chang, P. Knight and A. J. B. Vincent, "Microstructural development in equiatomic multicomponent alloys," *Materials Science and Engineering: A,* 375–377 (2004) 213-218. (doi: http://dx.doi.org/10.1016/j.msea.2003.10.257)

[9] M.-H. Tsai, R.-C. Tsai, T. Chang and W.-F. Huang, "Intermetallic Phases in High-Entropy Alloys: Statistical Analysis of their Prevalence and Structural Inheritance," *Metals,* 9 (2019). (doi: https://doi.org/10.3390/met9020247)

[10] J. Jiang and X. Luo, "High temperature oxidation behavior of AlCuTiFeNiCr high-entropy alloy," *Advanced Materials Research,* 652-654 (2013) 1115-1118. (doi: https://doi.org/10.4028/www.scientific.net/AMR.652-654.1115)

[11] P. K. Huang, J. W. Yeh, T. T. Shun and S. K. Chen, "Multi-Principal-Element Alloys with Improved Oxidation and Wear Resistance for Thermal Spray Coating," *Advanced Engineering Materials,* 6 (2004) 74-78. (doi: https://doi.org/10.1002/adem.200300507)

[12] C. M. Liu, H. M. Wang, S. Q. Zhang, H. B. Tang and A. L. Zhang, "Microstructure and oxidation behavior of new refractory high entropy alloys," *Journal of Alloys and Compounds,* 583 (2014) 162-169. (doi: http://dx.doi.org/10.1016/j.jallcom.2013.08.102)

[13] H. Zhang, Q. T. Wang, Q. H. Tang and P. Q. Dai, "High temperature oxidation property of $Al_{0.5}FeCoCrNi(Si_{0.2}, Ti_{0.5})$ high entropy alloys," *Corrosion and Protection,* 34 (2013) 561-565.

[14] O. N. Senkov, S. V. Senkova, D. M. Dimiduk, C. Woodward and D. B. Miracle, "Oxidation behavior of a refractory $NbCrMo_{0.5}Ta_{0.5}TiZr$ alloy," *Journal of Materials Science,* 47 (2012) 6522-6534. (doi: https://doi.org/10.1007/s10853-012-6582-0)

[15] C. Huang, Y. Zhang, J. Shen and R. Vilar, "Thermal stability and oxidation resistance of laser clad TiVCrAlSi high entropy alloy coatings on Ti-6Al-4V alloy," *Surface and Coatings Technology,* 206 (2011) 1389-1395. (doi: https://doi.org/10.1016/j.surfcoat.2011.08.063)

[16] S.-T. Chen, W.-Y. Tang, Y.-F. Kuo, S.-Y. Chen, C.-H. Tsau, T.-T. Shun and J.-W. Yeh, "Microstructure and properties of age-hardenable $Al_xCrFe_{1.5}MnNi_{0.5}$ alloys," *Materials Science and Engineering: A,* 527 (2010) 5818-5825. (doi: http://dx.doi.org/10.1016/j.msea.2010.05.052)

[17] M.-H. Chuang, M.-H. Tsai, W.-R. Wang, S.-J. Lin and J.-W. Yeh, "Microstructure and wear behavior of $Al_xCo_{1.5}CrFeNi_{1.5}Ti_y$ high-entropy alloys," *Acta Materialia,* 59 (2011) 6308-6317. (doi: https://doi.org/10.1016/j.actamat.2011.06.041)

[18] C.-C. Juan, C.-Y. Hsu, C.-W. Tsai, W.-R. Wang, T.-S. Sheu, J.-W. Yeh and S.-K. Chen, "On microstructure and mechanical performance of $AlCoCrFeMo_{0.5}Ni_x$ high-entropy alloys," *Intermetallics,* 32 (2013) 401-407. (doi: http://dx.doi.org/10.1016/j.intermet.2012.09.008)

[19] Y. Zhang, X. Yang and P. K. Liaw, "Alloy Design and Properties Optimization of High-Entropy Alloys," *JOM,* 64 (2012) 830-838. (doi: https://doi.org/10.1007/s11837-012-0366-5)

[20] H. Duan, Y. Wu, M. Hua, C. Yuan, D. Wang, J. Tu, H. Kou and J. Li, "Tribological properties of AlCoCrFeNiCu high-entropy alloys in hydrogen peroxide solution and in oil lubricant," *Wear,* 297 (2013) 1045-1051. (doi: https://doi.org/10.1016/j.wear.2012.11.014)

[21] J. C. Huang, "Evaluation of tribological behavior of Al-Co-Cr-Fe-Ni high entropy alloys using molecular dynamics simulation," *Scanning,* 34 (2012) 325-331. (doi: https://doi.org/10.1002/sca.21006)

[22] N. T. B. N. Koundinya, C. S. Babu, K. Sivaprasad, P. Susila, N. K. Babu and J. Baburao, "Phase evolution and thermal analysis of nanocrystalline AlCrCuFeNiZn high entropy alloy produced by mechanical alloying," *Journal of Materials Engineering and Performance,* 22 (2013) 3077-3084. (doi: https://doi.org/10.1007/s11665-013-0580-5)

[23] T. M. Butler, J. P. Alfano, R. L. Martens and M. L. Weaver, "High-Temperature Oxidation Behavior of Al-Co-Cr-Ni-(Fe or Si) Multicomponent High-Entropy Alloys," *JOM,* 67 (2015) 246-259. (doi: https://doi.org/10.1007/s11837-014-1185-7)

[24] B. Gorr, M. Azim, H. J. Christ, T. Mueller, D. Schliephake and M. Heilmaier, "Phase equilibria, microstructure, and high temperature oxidation resistance of novel refractory high-entropy alloys," *Journal of Alloys and Compounds,* 624 (2015) 270-278. (doi: http://dx.doi.org/10.1016/j.jallcom.2014.11.012)

[25] H. M. Daoud, A. M. Manzoni, R. Volkl, N. Wanderka and U. Glatzel, "Oxidation behavior of $Al_8Co_{17}Cr_{17}Cu_8Fe_{17}Ni_{33}$, $Al_{23}Co_{15}Cr_{23}Cu_8Fe_{15}Ni_{15}$, and $Al_{17}Co_{17}Cr_{17}Cu_{17}Fe_{17}Ni_{17}$ compositionally complex alloys (high-entropy alloys) at elevated temperatures in air," *Advanced Engineering Materials,* 17 (2015) 1134-1141. (doi: https://doi.org/10.1002/adem.201500179)

[26] G. R. Holcomb, J. Tylczak and C. Carney, "Oxidation of CoCrFeMnNi High Entropy Alloys," *JOM,* (2015). (doi: https://doi.org/10.1007/s11837-015-1517-2)

[27] Y.-X. Liu, C.-Q. Cheng, J.-L. Shang, R. Wang, P. Li and J. Zhao, "Oxidation behavior of high-entropy alloys $Al_xCoCrFeNi$ (x=0.15, 0.4) in supercritical water and comparison

with HR3C steel," *Transactions of Nonferrous Metals Society of China,* 25 (2015) 1341-1351. (doi: http://dx.doi.org/10.1016/S1003-6326(15)63733-5)
[28] T. M. Butler, "High Entropy Alloys: Oxidation," in "Encyclopedia of Materials: Metals and Alloys", edited by F. G. Caballero (Elsevier, Oxford, 2022) p. 522-532.
[29] Y. Wei, Y. Fu, Z.-m. Pan, Y.-c. Ma, H.-x. Cheng, Q.-c. Zhao, H. Luo and X.-g. Li, "Influencing factors and mechanism of high-temperature oxidation of high-entropy alloys: A review," *International Journal of Minerals, Metallurgy and Materials,* 28 (2021) 915-930. (doi: https://doi.org/10.1007/s12613-021-2257-7)
[30] B. R. Anne, S. Shaik, M. Tanaka and A. Basu, "A crucial review on recent updates of oxidation behavior in high entropy alloys," *SN Applied Sciences,* 3 (2021) 366. (doi: https://doi.org/10.1007/s42452-021-04374-1)
[31] X. Zhang, N. Zhang, B. Xing and S. Yin, "An assessment of the high-temperature oxidation resistance of selected thermal sprayed high entropy alloy coatings," *Journal of Thermal Spray Technology,* 31 (2022) 1386-1403. (doi: https://doi.org/10.1007/s11666-022-01352-w)
[32] S. Veselkov, O. Samoilova, N. Shaburova and E. Trofimov, "High-Temperature Oxidation of High-Entropic Alloys: A Review," *Materials (Basel, Switzerland),* 14 (2021) 2595. (doi: https://doi.org/10.3390/ma14102595)
[33] A. Meghwal, A. Anupam, B. S. Murty, C. C. Berndt, R. S. Kottada and A. S. M. Ang, "Thermal spray high-entropy alloy coatings: a review," *Journal of Thermal Spray Technology,* 29 (2020) 857-893. (doi: http://dx.doi.org/10.1007/s11666-020-01047-0)
[34] S.-Y. Chang, C.-E. Li, Y.-C. Huang, H.-F. Hsu, J.-W. Yeh and S.-J. Lin, "Structural and thermodynamic factors of suppressed interdiffusion kinetics in multi-component high-entropy materials," *Scientific Reports,* 4 (2014) 4162. (doi: https://doi.org/10.1038/srep04162)
[35] K. Y. Tsai, M. H. Tsai and J. W. Yeh, "Sluggish diffusion in Co–Cr–Fe–Mn–Ni high-entropy alloys," *Acta Materialia,* 61 (2013) 4887-4897. (doi: http://dx.doi.org/10.1016/j.actamat.2013.04.058)
[36] D. L. Beke and G. Erdélyi, "On the diffusion in high-entropy alloys," *Materials Letters,* 164 (2016) 111-113. (doi: http://dx.doi.org/10.1016/j.matlet.2015.09.028)
[37] T. M. Butler and M. L. Weaver, "Investigation of the Microstructures and Oxidation Behavior of AlNiCoCrFe High-Entropy Alloys," in Contributed Papers from Materials Science & Technology (MS&T) 2015 (TMS, Columbus, OH, 2015) p. 1257-1264.
[38] T. M. Butler and M. L. Weaver, "Oxidation behavior of arc melted AlCoCrFeNi multi-component high entropy alloys," *Journal of Alloys and Compounds,* 674 (2016) 229-244. (doi: https://doi.org/10.1016/j.jallcom.2016.02.257)
[39] T. Butler and M. Weaver, "Influence of annealing on the microstructures and oxidation behaviors of $Al_8(CoCrFeNi)_{92}$, $Al_{15}(CoCrFeNi)_{85}$, and $Al_{30}(CoCrFeNi)_{70}$ high-entropy alloys," *Metals,* 6 (2016) 222. (doi: https://doi.org/10.3390/met6090222)
[40] D. Tomus and H. P. Ng, "In situ lift-out dedicated techniques using FIB–SEM system for TEM specimen preparation," *Micron,* 44 (2013) 115-119. (doi: http://dx.doi.org/10.1016/j.micron.2012.05.006)
[41] FEI-Company, ES Vision, (2004).
[42] C. S. Tedmon, "The effect of oxide volatilization on the oxidation kinetics of Cr and Fe-Cr alloys," *Journal of the Electrochemical Society,* 113 (1966) 766-768. (doi: https://doi.org/10.1149/1.2424115)

[43] P. Kofstad, High Temperature Corrosion, (Elsevier Applied Science, New York, 1988).
[44] W. S. Rasband, ImageJ, (U.S. National Institutes of Health, Bethesda, MD, USA, 1997-2015).
[45] R. M. German, Powder Metallurgy & Particular Materials Processing, (Metal Powder Industries Federation, Princeton, 2005).
[46] W.-R. Wang, W.-L. Wang and J.-W. Yeh, "Phases, microstructure and mechanical properties of $Al_xCoCrFeNi$ high-entropy alloys at elevated temperatures," *Journal of Alloys and Compounds,* 589 (2014) 143-152. (doi: http://dx.doi.org/10.1016/j.jallcom.2013.11.084)
[47] W.-R. Wang, W.-L. Wang, S.-C. Wang, Y.-C. Tsai, C.-H. Lai and J.-W. Yeh, "Effects of Al addition on the microstructure and mechanical property of $Al_xCoCrFeNi$ high-entropy alloys," *Intermetallics,* 26 (2012) 44-51. (doi: http://dx.doi.org/10.1016/j.intermet.2012.03.005)
[48] Y. P. Wang, B. S. Li, M. X. Ren, C. Yang and H. Z. Fu, "Microstructure and compressive properties of AlCrFeCoNi high entropy alloy," *Materials Science and Engineering: A,* 491 (2008) 154-158. (doi: http://dx.doi.org/10.1016/j.msea.2008.01.064)
[49] U. Krupp and H. J. Christ, "Selective oxidation and internal nitridation during high-temperature exposure of single-crystalline nickel-base superalloys," *Metallurgical and Materials Transactions A,* 31 (2000) 47-56. (doi: http://dx.doi.org/10.1007/s11661-000-0051-0)
[50] J. Hall, K. Hellström, J. E. Svensson, M. Norell, M. Lundberg, T. Helander and L. G. Johansson, "The initial oxide scale development on a model FeNiCrAl Alloy at 900 °C in dry and humid atmosphere: a detailed investigation," *Oxidation of Metals,* 82 (2014) 225-247. (doi: http://dx.doi.org/10.1007/s11085-014-9489-0)
[51] A. Manzoni, H. Daoud, S. Mondal, S. van Smaalen, R. Völkl, U. Glatzel and N. Wanderka, "Investigation of phases in Al23Co15Cr23Cu8Fe15Ni16 and Al8Co17Cr17Cu8Fe17Ni33 high entropy alloys and comparison with equilibrium phases predicted by Thermo-Calc," *Journal of Alloys and Compounds,* 552 (2013) 430-436. (doi: http://dx.doi.org/10.1016/j.jallcom.2012.11.074)
[52] C. Ng, S. Guo, J. Luan, S. Shi and C. T. Liu, "Entropy-driven phase stability and slow diffusion kinetics in an Al0.5CoCrCuFeNi high entropy alloy," *Intermetallics,* 31 (2012) 165-172. (doi: http://dx.doi.org/10.1016/j.intermet.2012.07.001)
[53] C. Zhang, F. Zhang, S. Chen and W. Cao, "Computational Thermodynamics Aided High-Entropy Alloy Design," *JOM,* 64 (2012) 839-845. (doi: https://doi.org/10.1007/s11837-012-0365-6)
[54] F. Zhang, C. Zhang, S. L. Chen, J. Zhu, W. S. Cao and U. R. Kattner, "An understanding of high entropy alloys from phase diagram calculations," *Calphad,* 45 (2014) 1-10. (doi: http://dx.doi.org/10.1016/j.calphad.2013.10.006)
[55] L. Klein, A. Zendegani, M. Palumbo, S. G. Fries and S. Virtanen, "First approach for thermodynamic modelling of the high temperature oxidation behaviour of ternary γ′-strengthened Co–Al–W superalloys," *Corrosion Science,* 89 (2014) 1-5. (doi: http://dx.doi.org/10.1016/j.corsci.2014.08.016)
[56] S. Salam, P. Y. Hou, Y. D. Zhang, H. Lan, H. F. Wang, C. Zhang and Z. G. Yang, "Element accumulation beneath the scale/alloy interface of a CoNiCrAlReY alloy," *Corrosion Science,* 89 (2014) 318-325. (doi: http://dx.doi.org/10.1016/j.corsci.2014.09.015)

[57] C. Jang, D. Kim, D. Kim, I. Sah, W.-S. Ryu and Y.-s. Yoo, "Oxidation behaviors of wrought nickel-based superalloys in various high temperature environments," *Transactions of Nonferrous Metals Society of China,* 21 (2011) 1524-1531. (doi: http://dx.doi.org/10.1016/S1003-6326(11)60891-1)
[58] C. S. Giggins and F. S. Pettit, "Oxidation of Ni-Cr-Al alloys between 1000°C and 1200°C," *Journal of the Electrochemical Society,* 118 (1971) 1782-1790. (doi: http://dx.doi.org/10.1149/1.2407837)
[59] F. H. Stott, G. C. Wood and M. G. Hobby, "A comparison of the oxidation behavior of Fe-Cr-Al, Ni-Cr-Al, and Co-Cr-Al alloys," *Oxidation of Metals,* 3 (1971) 103-113. (doi: https://doi.org/10.1007/BF00603481)
[60] F. H. Stott, "Oxidation of alumina-forming alloys," *Materials Science Forum,* 251-254 (1997) 19-32. (doi: https://doi.org/10.4028/www.scientific.net/MSF.251-254.19)
[61] F. H. Stott and G. C. Wood, "The mechanism of oxidation of Ni-Cr-Al alloys at 1000°–1200°C," *Corrosion Science,* 11 (1971) 799-812. (doi: http://dx.doi.org/10.1016/S0010-938X(71)80044-6)
[62] G. R. Wallwork and A. Z. Hed, "Some limiting factors in the use of alloys at high temperatures," *Oxidation of Metals,* 3 (1971) 171-184. (doi: https://doi.org/10.1007/BF00603485)
[63] N. Birks, G. H. Meier and F. S. Pettit, High-Temperature Oxidation of Metals, 2nd Edition, (Cambridge University Press, Cambridge, UK, 2006).
[64] M. W. Brumm and H. J. Grabke, "The oxidation behaviour of NiAl-I. Phase transformations in the alumina scale during oxidation of NiAl and NiAl-Cr alloys," *Corrosion Science,* 33 (1992) 1677-1690. (doi: http://dx.doi.org/10.1016/0010-938X(92)90002-K)
[65] A. Faraji, M. Farvizi, T. Ebadzadeh and H. S. Kim, "Microstructure, wear performance, and mechanical properties of spark plasma-sintered AlCoCrFeNi high-entropy alloy after heat treatment," *Intermetallics,* 149 (2022) 107656. (doi: https://doi.org/10.1016/j.intermet.2022.107656)
[66] Ł. Rogal, Z. Szklarz, P. Bobrowski, D. Kalita, G. Garzeł, A. Tarasek, M. Kot and M. Szlezynger, "Microstructure and Mechanical Properties of Al–Co–Cr–Fe–Ni Base High Entropy Alloys Obtained Using Powder Metallurgy," *Metals and Materials International,* 25 (2019) 930-945. (doi: 10.1007/s12540-018-00236-5)
[67] Z. J. Shi, Z. B. Wang, X. D. Wang, S. Zhang and Y. G. Zheng, "Effect of thermally induced B2 phase on the corrosion behavior of an $Al_{0.3}$CoCrFeNi high entropy alloy," *Journal of Alloys and Compounds,* 903 (2022) 163886. (doi: https://doi.org/10.1016/j.jallcom.2022.163886)
[68] K. Yamanaka, H. Shiratori, M. Mori, K. Omura, T. Fujieda, K. Kuwabara and A. Chiba, "Corrosion mechanism of an equimolar AlCoCrFeNi high-entropy alloy additively manufactured by electron beam melting," *npj Materials Degradation,* 4 (2020) 24. (doi: https://doi.org/10.1038/s41529-020-00127-4)
[69] M. Garg, H. S. Grewal, R. K. Sharma and H. S. Arora, "Improving the high temperature oxidation resistance of high entropy alloy by surface modification," *Corrosion Reviews,* 41 (2023) 39-56. (doi: doi:10.1515/corrrev-2022-0011)
[70] M. Garg, H. S. Grewal, R. K. Sharma, B. Gwalani and H. S. Arora, "High oxidation resistance of AlCoCrFeNi high entropy alloy through severe shear deformation

processing," *Journal of Alloys and Compounds,* 917 (2022) 165385. (doi: https://doi.org/10.1016/j.jallcom.2022.165385)
[71] M. Garg, H. S. Grewal, R. K. Sharma, B. Gwalani and H. S. Arora, "Limiting oxidation of high entropy alloy via high strain-rate deformation: Insights from electrochemical impedance spectroscopy," *Materials Chemistry and Physics,* 294 (2023) 127017. (doi: https://doi.org/10.1016/j.matchemphys.2022.127017)
[72] A. Erdogan, S. E. Sunbul, K. Icin and K. M. Doleker, "Microstructure, wear and oxidation behavior of AlCrFeNiX (X = Cu, Si, Co) high entropy alloys produced by powder metallurgy," *Vacuum,* 187 (2021) 110143. (doi: https://doi.org/10.1016/j.vacuum.2021.110143)
[73] A. Anupam, S. Kumar, N. M. Chavan, B. S. Murty and R. S. Kottada, "First report on cold-sprayed AlCoCrFeNi high-entropy alloy and its isothermal oxidation," *Journal of Materials Research,* 34 (2019) 796-806. (doi: https://doi.org/10.1557/jmr.2019.38)

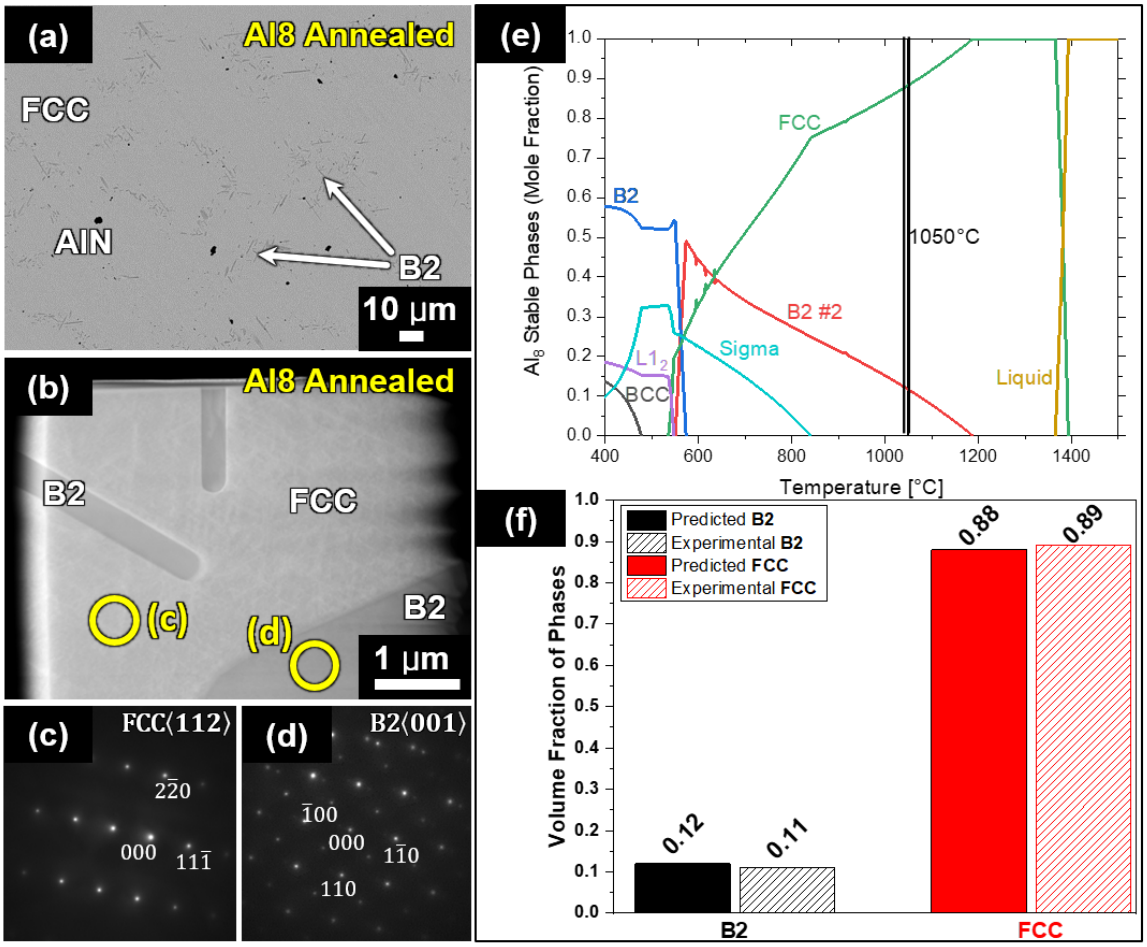

Figure 1. Figure 1. Representative BSE and STEM-HAADF images of the annealed Al_8 CCA (a)-(b) along with corresponding SADPs taken from each respective phase (c)-(d); thermodynamically calculated phase diagram for the Al_8 HEA using the TCHEA4 database in ThermoCalc (e); and bar plot of the predicted phase fractions along with those determined experimentally (f).

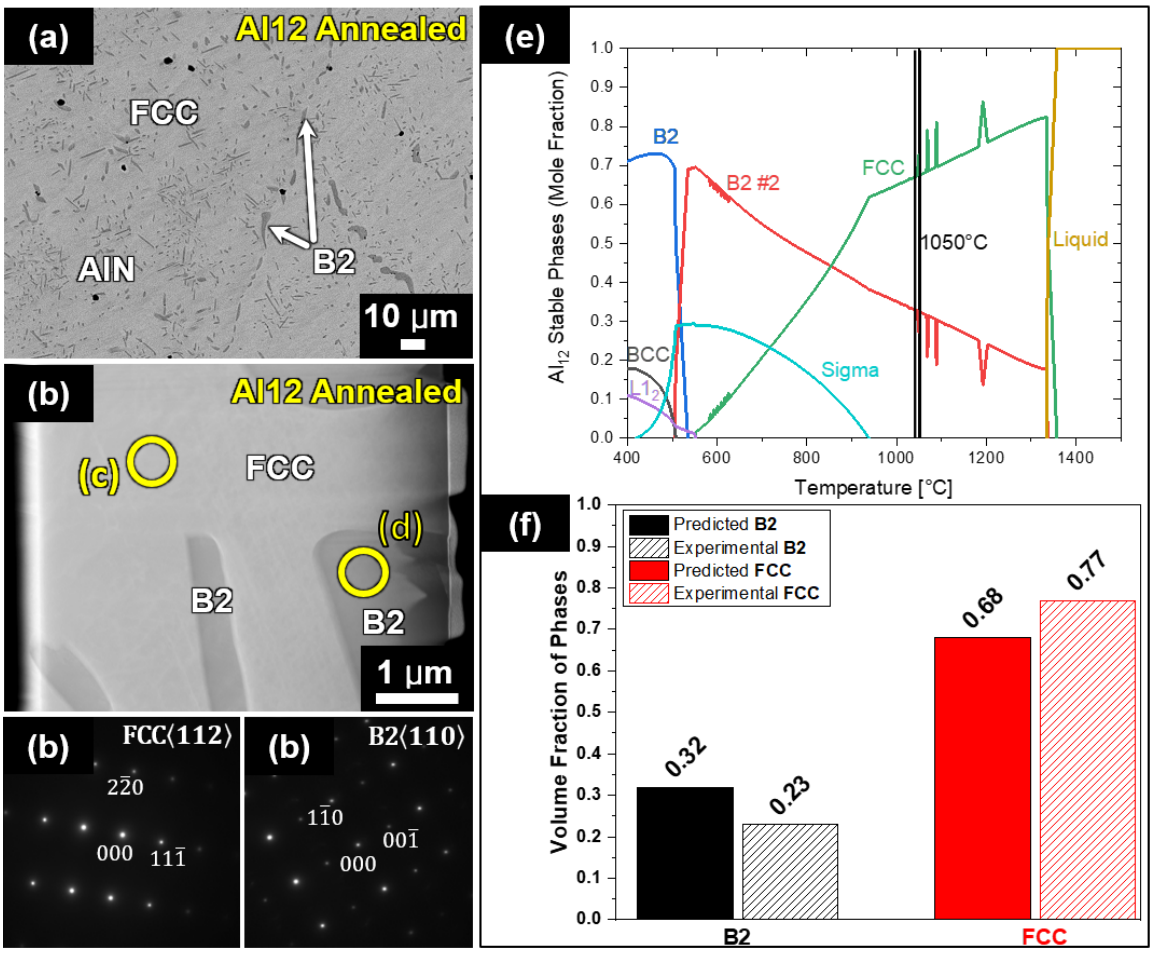

Figure 2. Representative BSE and STEM-HAADF images of the annealed Al_{12} CCA (a)-(b) along with corresponding SADPs taken from each respective phase (c)-(d); thermodynamically calculated phase diagram for the Al_{12} HEA using the TCHEA4 database in ThermoCalc (e); and bar plot of the predicted phase fractions along with those determined experimentally (f).

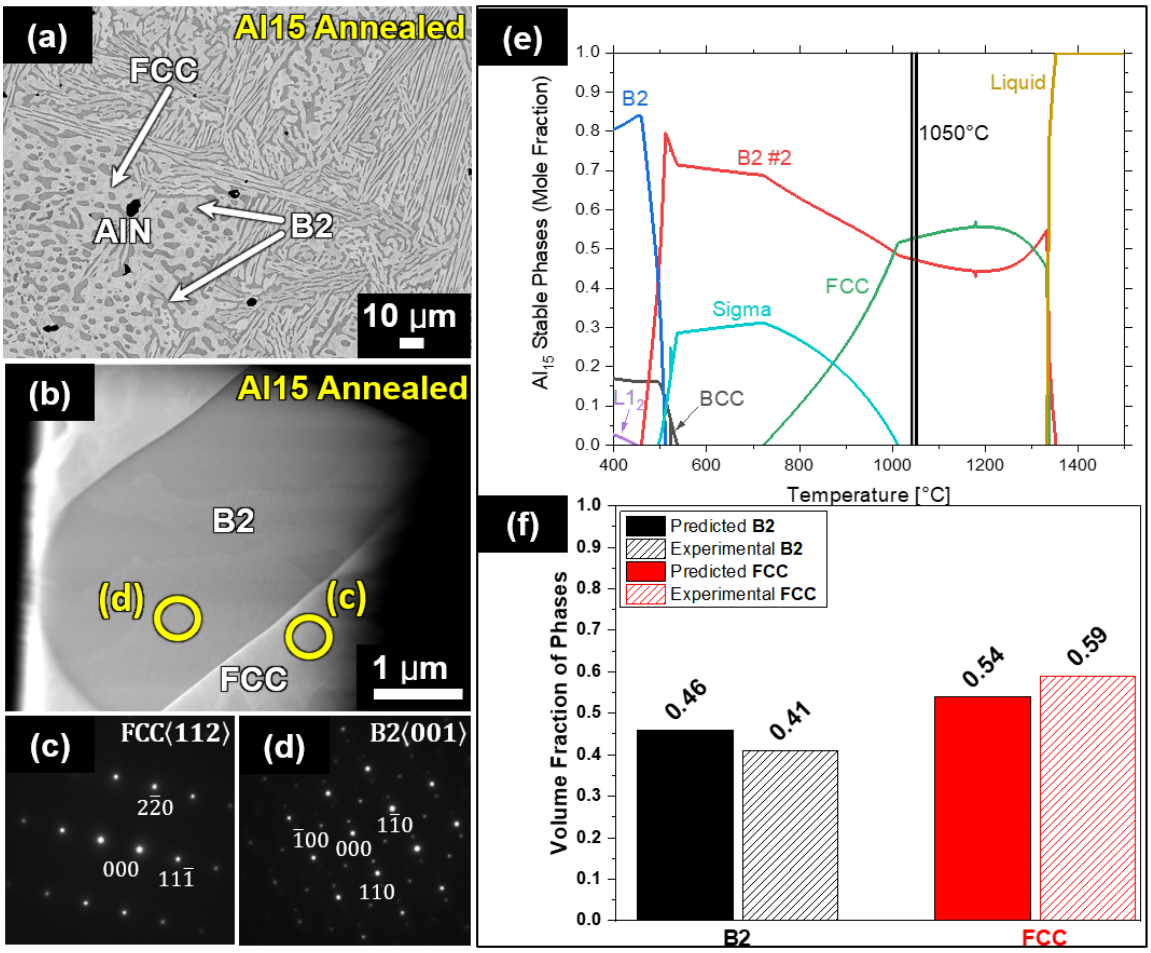

Figure 3. Representative BSE and STEM-HAADF images of the annealed Al_{15} CCA (a)-(b) along with corresponding SADPs taken from each respective phase (c)-(d); thermodynamically calculated phase diagram for the Al_{15} HEA using the TCHEA4 database in ThermoCalc (e); and bar plot of the predicted phase fractions along with those determined experimentally (f).

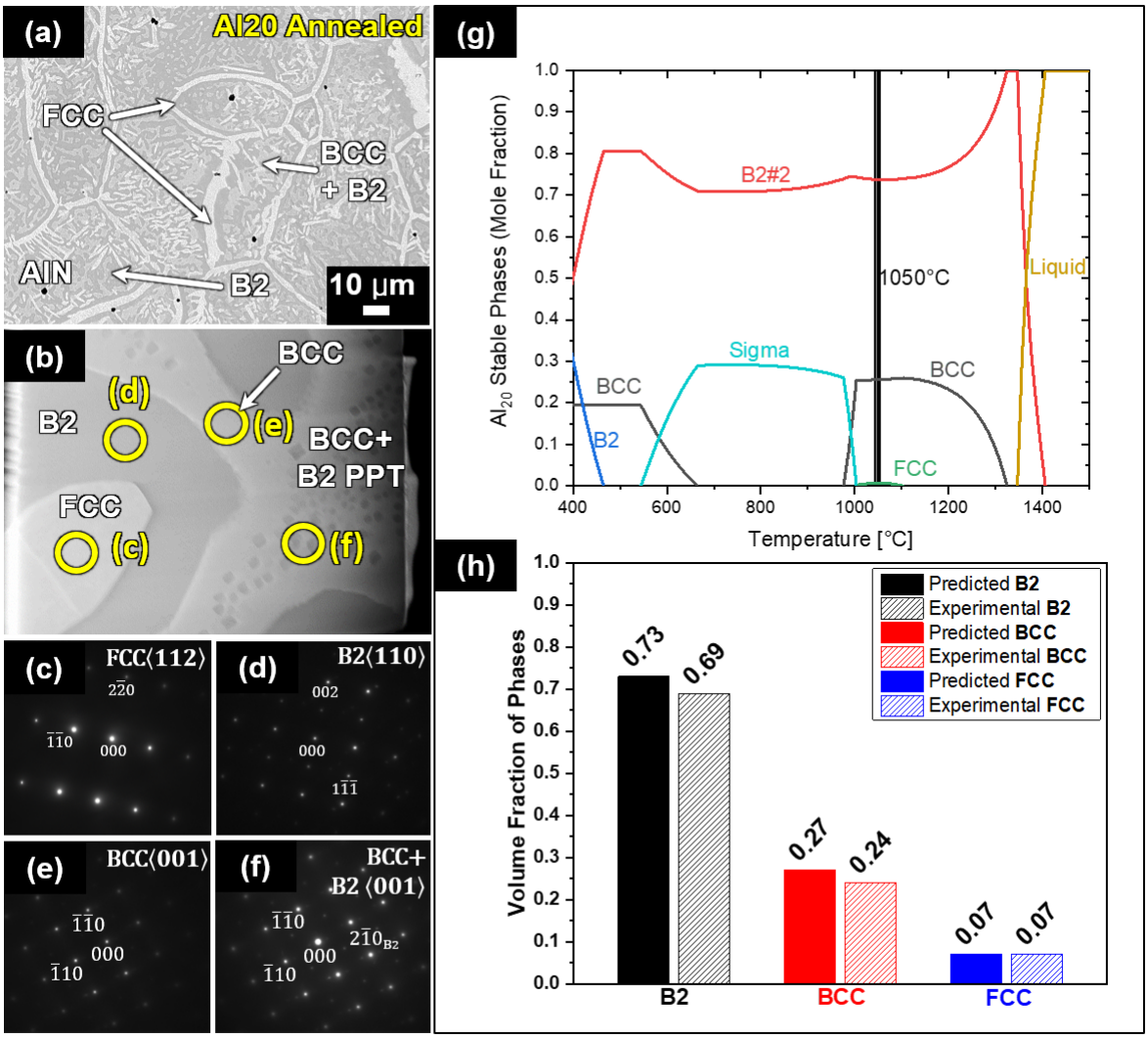

Figure 4. Representative BSE and STEM-HAADF images of the annealed Al_{20} CCA (a)-(b) along with corresponding SADPs taken from each respective phase (c)-(f); thermodynamically calculated phase diagram for the Al_{20} HEA using the TCHEA4 database in ThermoCalc (g); and bar plot of the predicted phase fractions along with those determined experimentally (h).

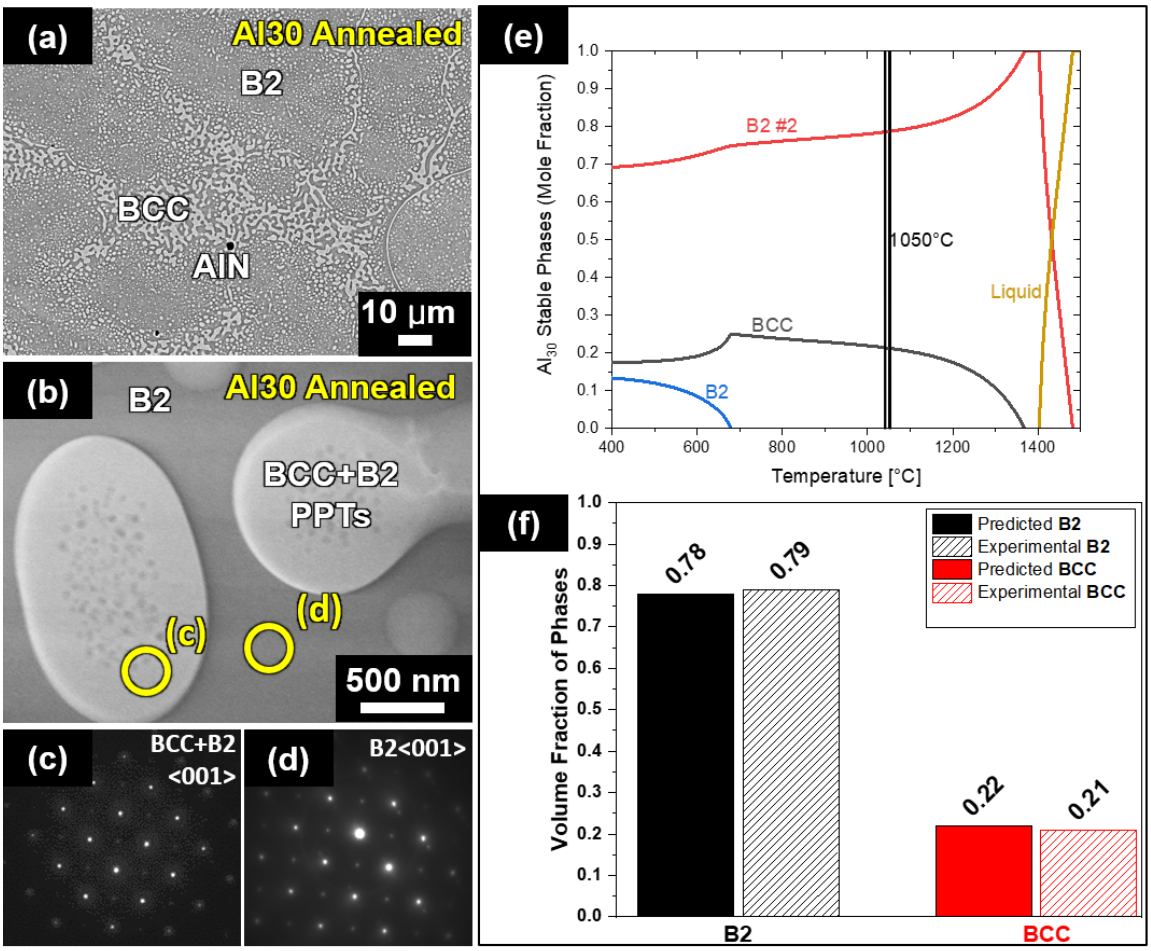

Figure 5. Representative BSE and STEM-HAADF images of the annealed Al_{30} CCA (a)-(b) along with corresponding SADPs taken from each respective phase (c)-(d); thermodynamically calculated phase diagram for the Al_{30} HEA using the TCHEA4 database in ThermoCalc (e); and bar plot of the predicted phase fractions along with those determined experimentally (f).

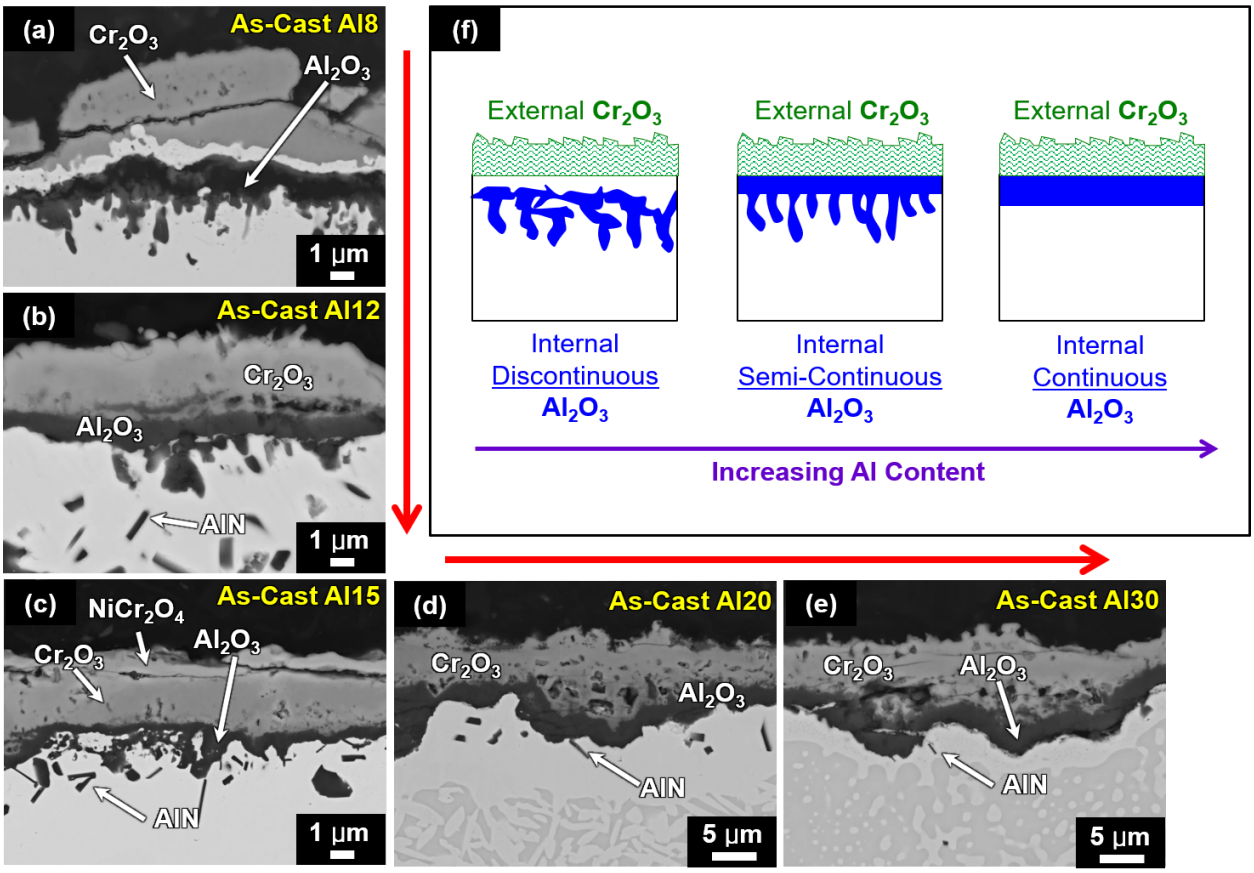

Figure 6. Cross-sectional BSE images of the as-cast Al_8, Al_{12}, Al_{15}, Al_{20}, and Al_{30} CCAs after 50 hours of oxidation at 1050°C in air (a)-(e), respectively; schematic of oxidation mechanisms for the as-cast CCAs (f).

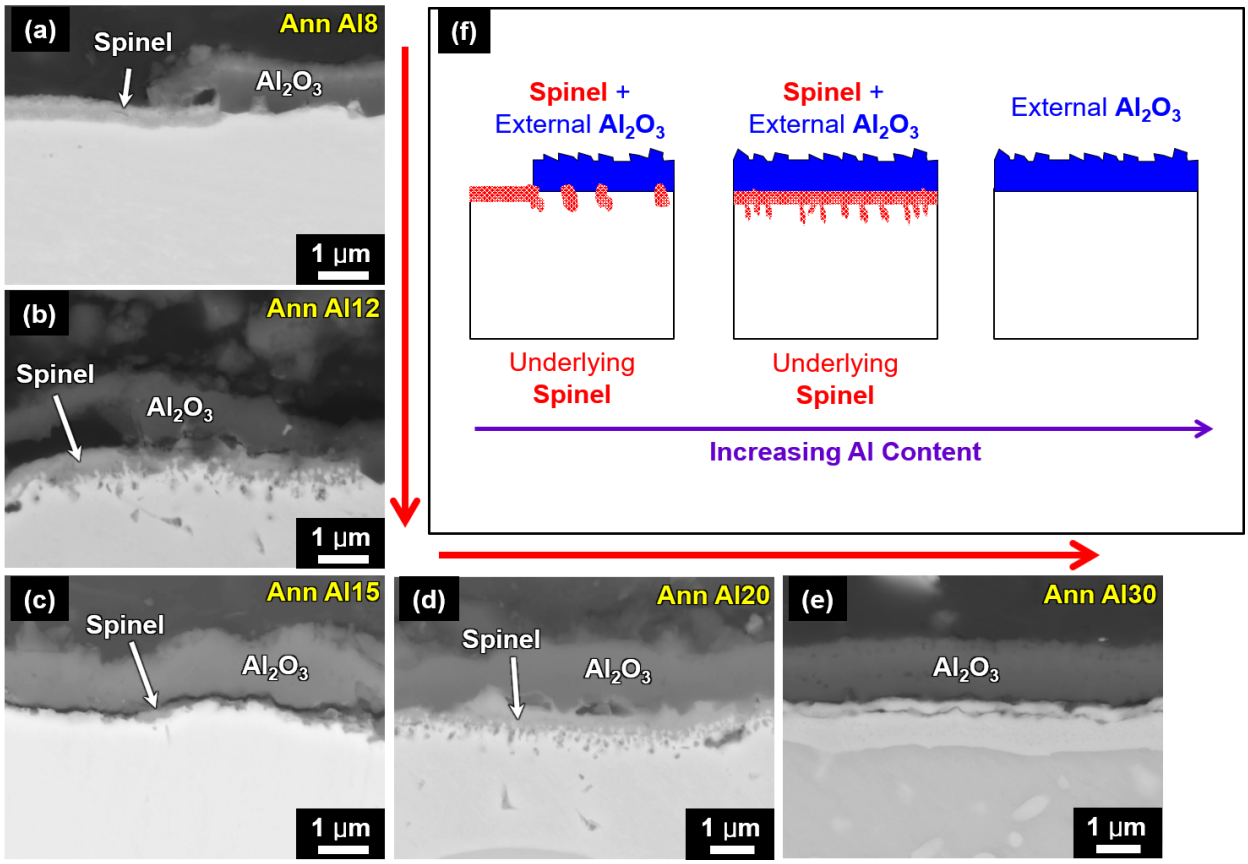

Figure 7. Cross-sectional BSE images of the annealed Al_8, Al_{12}, Al_{15}, Al_{20}, and Al_{30} CCAs after 50 hours of oxidation at 1050°C in air (a)-(e), respectively; schematic of oxidation mechanisms for the as-cast CCAs (f).

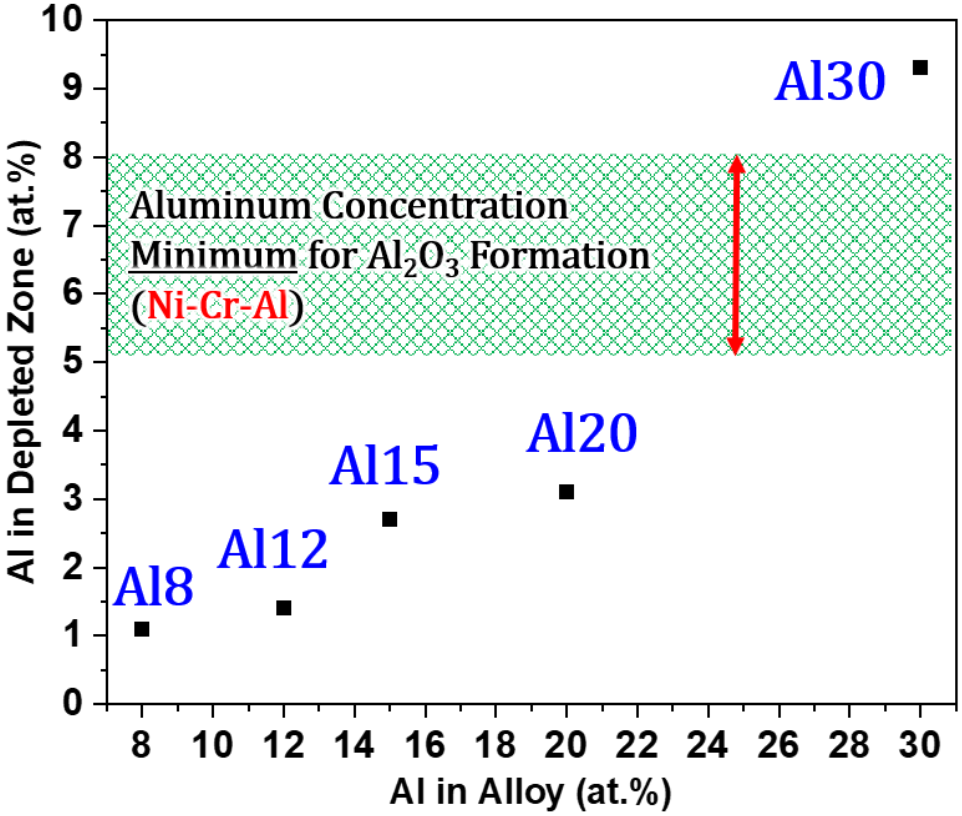

Figure 8. Plot of Al concentration in the depleted zones of the annealed / oxidized CCAs versus Al content in the Alloy. The respective window for the minimum concentration of Al required for Al2O3 formation in Ni-Cr-Al alloys is also shown.

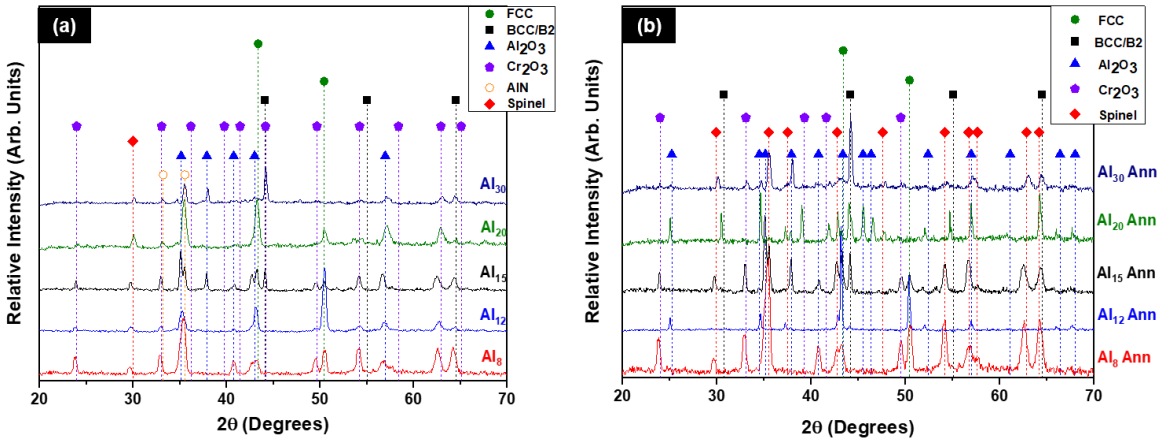

Figure 9. XRD patterns captured from the as-cast (a) and annealed CCAs (b) after 50 hours of oxidation at 1050°C in air.

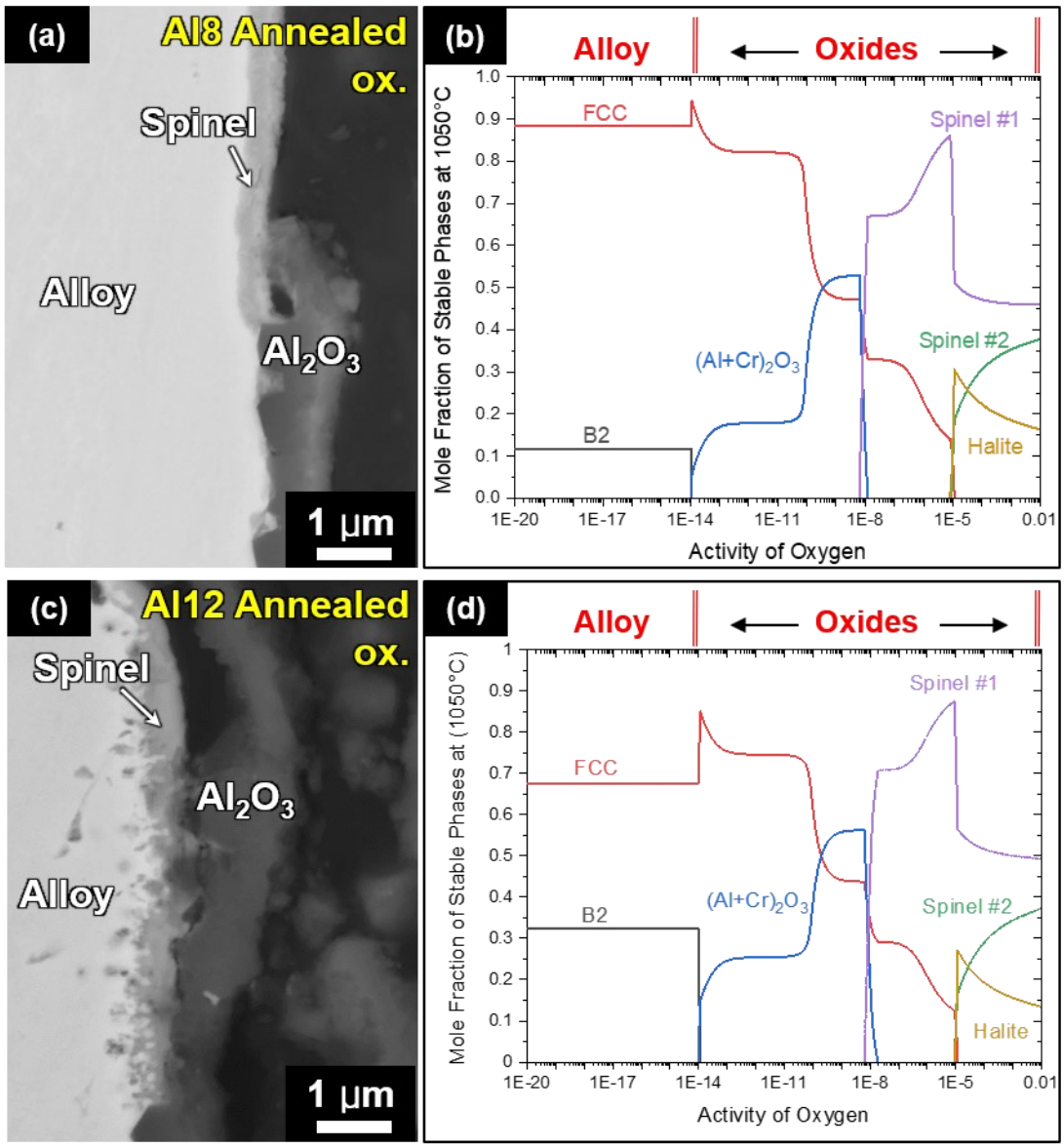

Figure 10. 90° Clockwise rotated BSE images of the annealed Al_8 and Al_{12} CCAs after 50 hours of oxidation (a) and (c), respectively; along with thermodynamically calculated 1050°C isothermal phase diagrams for the Al_8 and Al_{12} CCAs with varying oxygen activities (b) and (d), respectively. The calculations were performed using the TCNI9 Ni-based superalloys and TCHEA4 High Entropy Alloy databases in ThermoCalc.

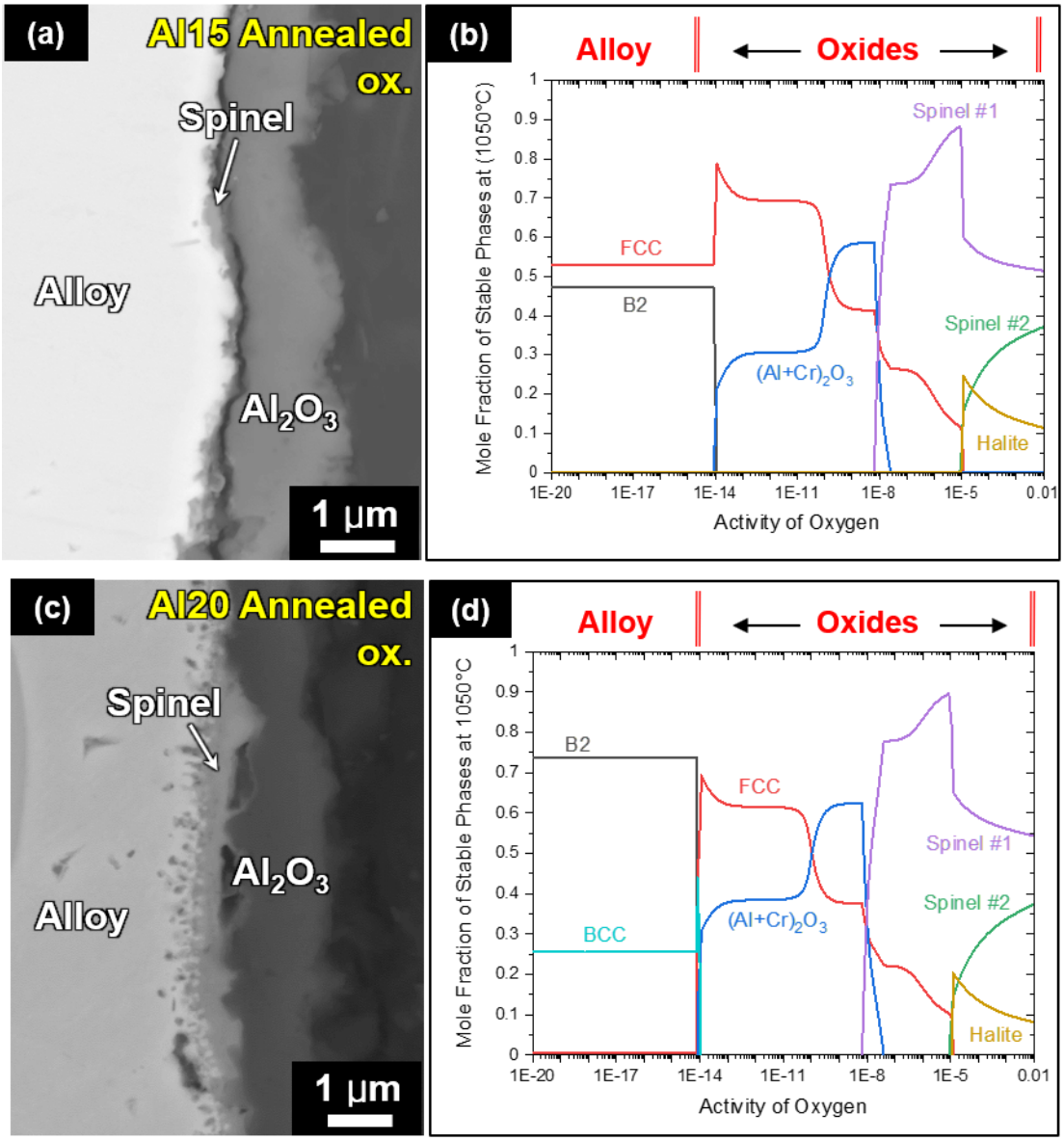

Figure 11. 90° Clockwise rotated BSE images of the annealed Al_{15} and Al_{20} CCAs after 50 hours of oxidation (a) and (c), respectively; along with thermodynamically calculated 1050°C isothermal phase diagrams for the Al_{15} and Al_{20} CCAs with varying oxygen activities (b) and (d), respectively. The calculations were performed using the TCNI9 Ni-based superalloys and TCHEA 4 High Entropy Alloy databases in ThermoCalc.

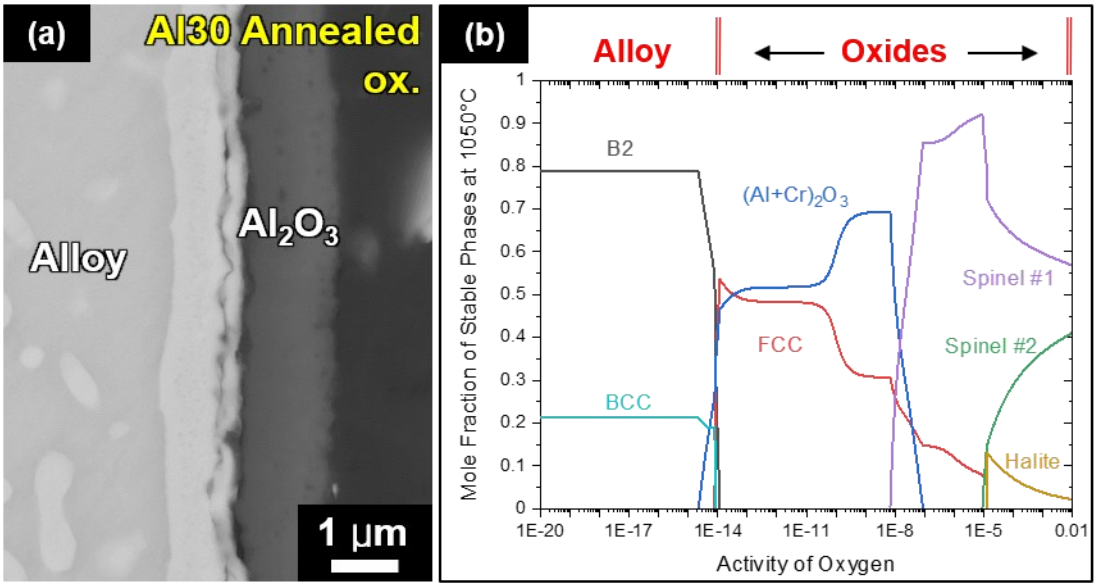

Figure 12. 90° Clockwise rotated BSE image of the annealed Al_{30} CCAs after 50 hours of oxidation (a) along with a corresponding thermodynamically calculated 1050°C isothermal phase diagram with varying oxygen activity (b). The calculation was performed using the TCNI9 Ni-based superalloys and TCHEA 4 High Entropy Alloy databases in ThermoCalc

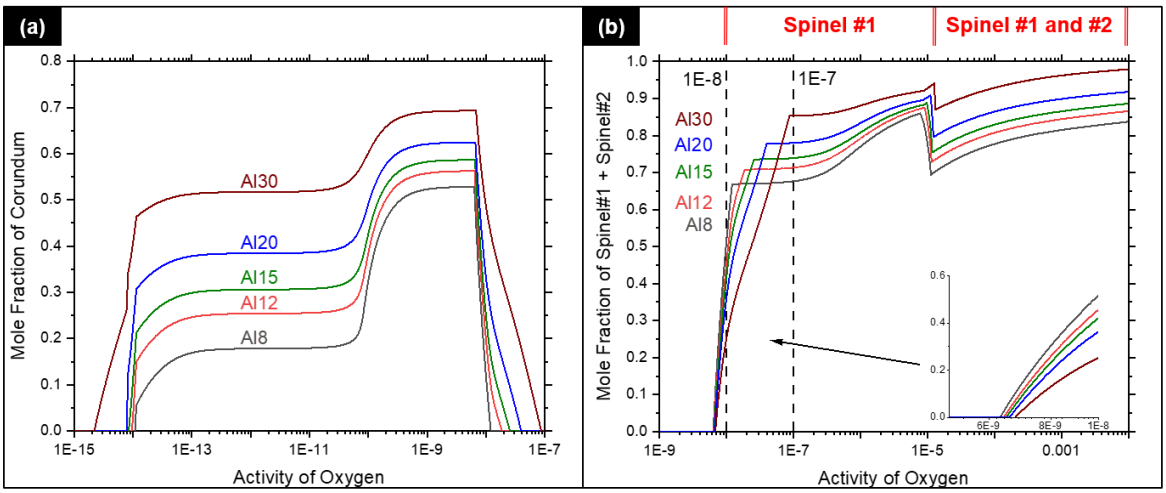

Figure 13. Comparison of corundum ($(Al+Cr)_2O_3$) (a) and combined spinel phases (b) formation range between each alloy composition with dashed lines bounding the activity of oxygen required for initiation. Spinel #1 and Spinel #2 are nominally CoCrAlO and NiFeO, respectively.

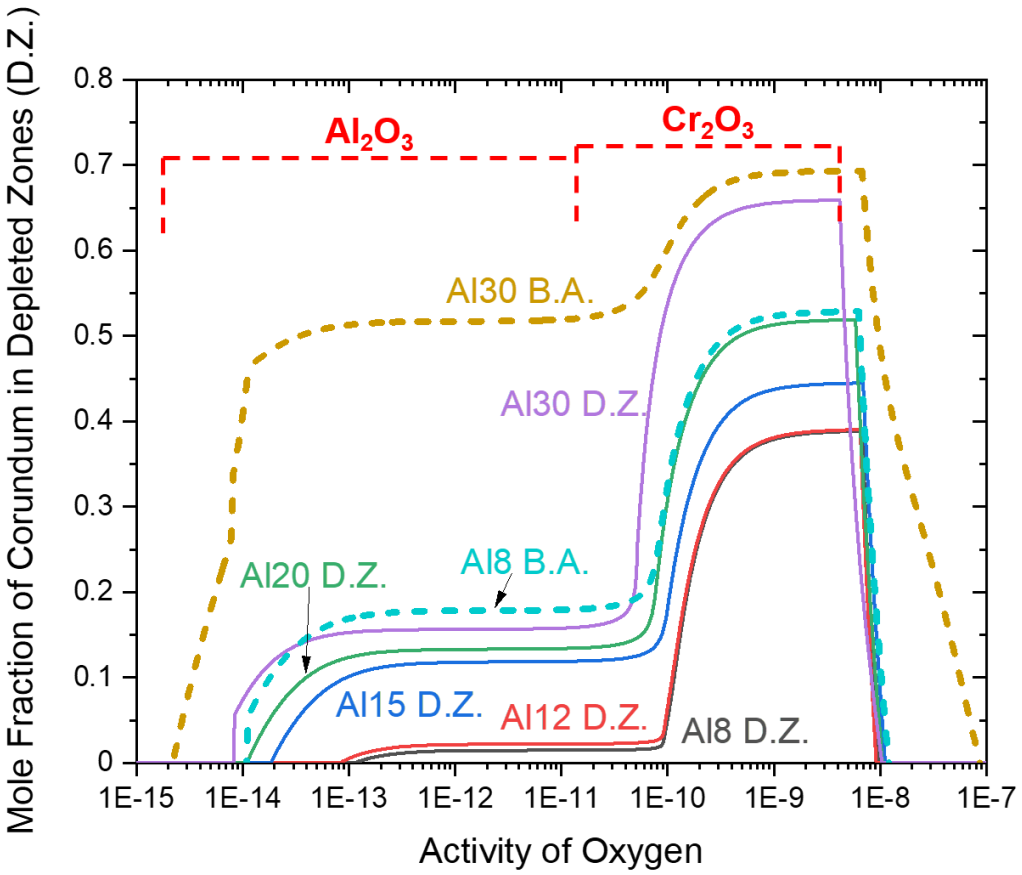

Figure 14. Comparative graph of corundum forming region for each alloy with B.A. designating base alloy compositions and D.Z. designating chemistries found in the depleted zone of each alloy.

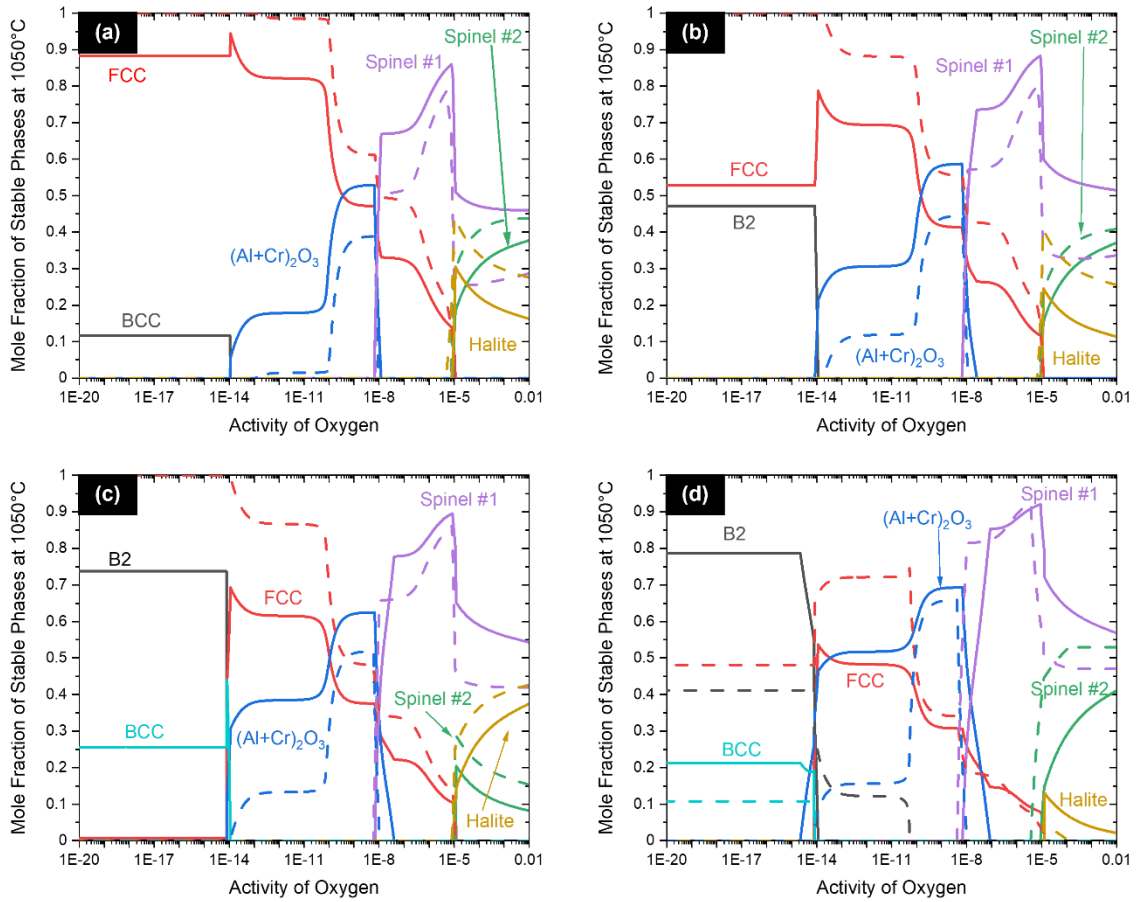

Figure 15. Predicted oxide road maps with base alloy composition represented by solid lines and the depleted alloy composition represented with dashed lines. A) Al_8, B) Al_{15}, C) Al_{20}, D) Al_{30}.

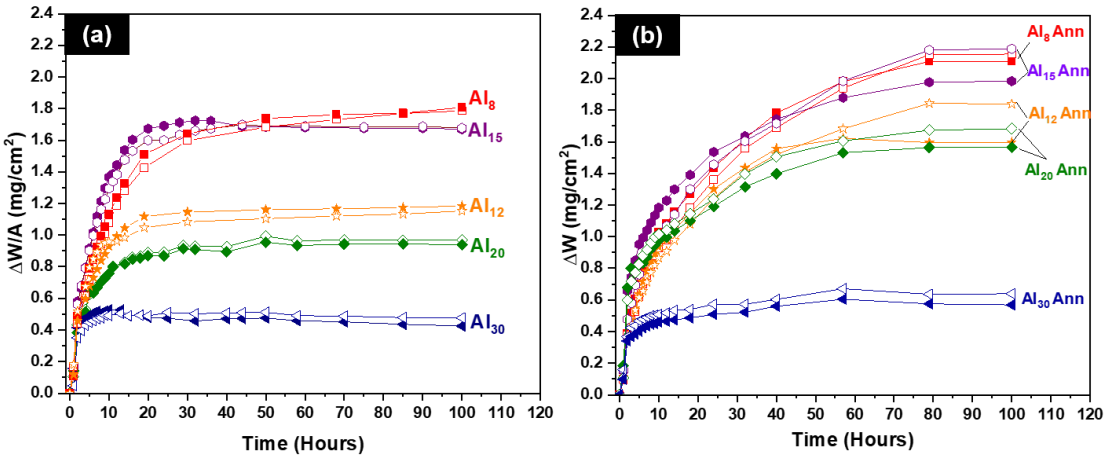

Figure 16. 1050°C oxidation mass change curves (normalized by surface area) as a function of time for the as-cast (a) and annealed (Ann) CCAs (b).

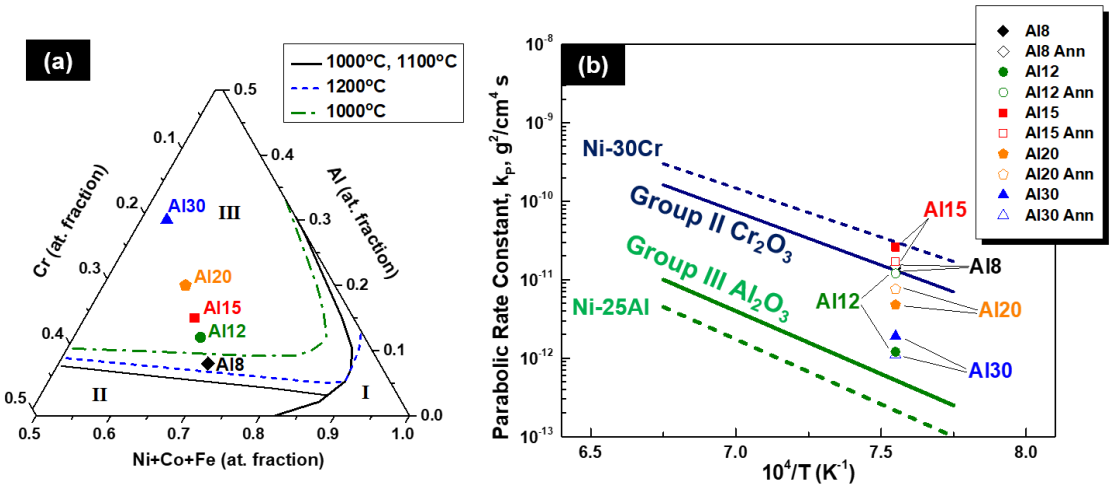

Figure 17. Schematic oxide formation map (a) along with the respective compositions of the CCAs in this study; and log plot of the parabolic oxide growth rate constants (k_P) for the CCAs in this study versus 10^4/T. For reference the corresponding regions observed for model Group II and Group III Ni-Cr-Al alloys is also shown.

Table 1. Overall compositions of the CCAs and the respective phase chemistries after annealing for 120 hr/1050°C determined via SEM-EDS (at.%). The thermodynamically predicted phase chemistries at 1050°C using the CALPHAD method are also shown for comparison.

Alloy	Phase	Al	Ni	Co	Cr	Fe
Al_8	**Overall**	**8.2 ± 0.2**	**22.2 ± 0.5**	**22.8 ± 0.2**	**24.0 ± 0.3**	**22.8 ± 0.2**
	FCC	**7.7 ± 0.2**	**21.9 ± 0.3**	**23.3 ± 0.1**	**24.2 ± 0.2**	**23.0 ± 0.3**
	FCC (Predicted)	**5.6**	**22.1**	**23.3**	**24.9**	**24.0**
	B2	**25.2 ± 2.2**	**30.5 ± 2.4**	**16.9 ± 1.0**	**13.0 ± 2.3**	**14.3 ± 1.3**
	B2 (Predicted)	**25.9**	**29.7**	**20.5**	**8.3**	**15.6**
Al_{12}	**Overall**	**12.1 ± 0.1**	**22.5 ± 0.6**	**21.7 ± 0.6**	**21.9 ± 0.1**	**21.8 ± 0.6**
	FCC	**7.5 ± 0.3**	**21.4 ± 0.3**	**23.2 ± 0.3**	**24.8 ± 0.2**	**22.8 ± 0.2**
	FCC (Predicted)	**5.3**	**18.9**	**22.6**	**28.2**	**24.9**
	B2	**32.0 ± 0.1**	**35.1 ± 0.2**	**14.9 ± 0.3**	**7.4 ± 0.1**	**10.6 ± 0.3**
	B2 (Predicted)	**26.0**	**28.3**	**20.7**	**9.2**	**15.8**
Al_{15}	**Overall**	**15.6 ± 0.1**	**20.5 ± 0.1**	**20.8 ± 0.1**	**21.9 ± 0.1**	**21.1 ± 0.1**
	FCC	**6.9 ± 0.2**	**16.5 ± 0.2**	**22.9 ± 0.5**	**28.1 ± 0.4**	**25.6 ± 0.5**
	FCC (Predicted)	**5.0**	**16.2**	**21.7**	**31.2**	**25.9**
	B2	**31.0 ± 0.6**	**29.4 ± 0.5**	**17.3 ± 0.4**	**10.0 ± 0.8**	**12.2 ± 0.6**
	B2 (Predicted)	**26.2**	**26.9**	**20.7**	**10.1**	**16.1**
Al_{20}	**Overall**	**20.2 ± 0.1**	**19.3 ± 0.1**	**19.7 ± 0.1**	**20.8 ± 0.2**	**20.1 ± 0.1**
	BCC	**7.4 ± 0.5**	**8.7 ± 0.3**	**19.2 ± 0.2**	**37.9 ± 0.7**	**26.7 ± 0.3**
	BCC (Predicted)	**3.8**	**5.9**	**15.7**	**48.0**	**26.5**
	FCC	**7.2 ± 0.1**	**13.4 ± 0.2**	**23.5 ± 0.3**	**27.5 ± 0.1**	**28.4 ± 0.2**
	FCC (Predicted)	**5.0**	**13.9**	**21.6**	**30.9**	**28.6**
	B2	**31.7 ± 0.2**	**26.6 ± 0.3**	**18.7 ± 0.1**	**9.6 ± 0.2**	**13.4 ± 0.3**
	B2 (Predicted)	**25.8**	**24.9**	**21.5**	**10.2**	**17.7**
Al_{30}	**Overall**	**29.2 ± 0.2**	**17.4 ± 0.1**	**17.6 ± 0.1**	**18.3 ± 0.1**	**17.6 ± 0.2**
	BCC	**11.7 ± 0.3**	**6.0 ± 0.7**	**13.3 ± 0.2**	**40.6 ± 0.1**	**28.2 ± 0.4**
	BCC (Predicted)	**7.8**	**1.2**	**6.2**	**58.5**	**26.3**
	B2	**35.5 ± 1.3**	**20.4 ± 0.9**	**18.2 ± 0.8**	**12.0 ± 2.1**	**13.9 ± 0.8**
	B2 (Predicted)	**35.9**	**21.9**	**20.1**	**6.4**	**15.1**

Table 2. Average parabolic oxide rate constants (k_P) calculated for the as-cast and annealed CCAs.

Alloy	Initial Condition	k_P (1) (g^2/cm^4 s)	Duration for k_P (1)	k_P (2) (g^2/cm^4 s)	Duration for k_P (2)	Primary Oxides
Al_8	As-cast	~ 2.5 x 10^{-11}	1 – 30 hours	~ 2.5 x 10^{-12}	30 – 100 hours	Cr_2O_3 / Al_2O_3
	Annealed	~ 2.2 x 10^{-11}	2 – 40 hours	~ 8.9 x 10^{-12}	40 – 80 hours	Al_2O_3 / Spinel
Al_{12}	As-cast	~ 1.9 x 10^{-12}	1 – 19 hours	~ 4.6 x 10^{-13}	19 – 100 hours	Cr_2O_3 / Al_2O_3
	Annealed	~ 1.6 x 10^{-11}	2 – 40 hours	~ 7.7 x 10^{-12}	40 – 80 hours	Al_2O_3 / Spinel
Al_{15}	As-cast	~ 4.7 x 10^{-11}	2 – 18 hours	~ 4.2 x 10^{-12}	19 – 36 hours	Cr_2O_3 / Al_2O_3
	Annealed	~ 2.6 x 10^{-11}	2 – 20 hours	~ 7.8 x 10^{-12}	20 – 80 hours	Al_2O_3 / Spinel
Al_{20}	As-cast	~ 8.1 x 10^{-12}	1 – 11 hours	~ 1.6 x 10^{-12}	12 – 50 hours	Cr_2O_3 / Al_2O_3
	Annealed	~ 1.1 x 10^{-11}	3 – 35 hours	~ 4.2 x 10^{-12}	35 – 80 hours	Al_2O_3 / Spinel
Al_{30}	As-cast	~ 1.9 x 10^{-12}	2 – 10 hours	--	--	Cr_2O_3 / Al_2O_3
	Annealed	~ 1.1 x 10^{-12}	5 – 80 hours	--	--	Al_2O_3